

Magnetorotational instability in protoplanetary discs

Raquel Salmeron¹^{★†} and Mark Wardle²

¹*School of Physics, University of Sydney, Sydney NSW 2006, Australia*

²*Physics Department, Macquarie University, Sydney NSW 2109, Australia*

Accepted 2005 March 31. Received 2005 March 28; in original form 2004 August 23

ABSTRACT

We investigate the linear growth and vertical structure of the magnetorotational instability (MRI) in weakly ionized, stratified accretion discs. The magnetic field is initially vertical and dust grains are assumed to have settled towards the mid-plane, so charges are carried by electrons and ions only. Solutions are obtained at representative radial locations from the central protostar for different choices of the initial magnetic field strength, sources of ionization, disc structure and configuration of the conductivity tensor.

The MRI is active over a wide range of magnetic field strengths and fluid conditions in low-conductivity discs. Moreover, no evidence was found of a low-limit field strength below which unstable modes do not exist. For the minimum-mass solar nebula model, incorporating cosmic ray ionization, perturbations grow at 1 au for $B \lesssim 8$ G. For a significant subset of these strengths ($200 \text{ mG} \lesssim B \lesssim 5$ G), the maximum growth rate is of the order of the ideal magnetohydrodynamic (MHD) rate (0.75Ω). Hall conductivity modifies the structure and growth rate of global unstable modes at 1 au for all magnetic field strengths that support MRI. As a result, at this radius, modes obtained with a full conductivity tensor grow faster and are active over a more extended cross-section of the disc than perturbations in the ambipolar diffusion limit. For relatively strong fields (e.g. $B \gtrsim 200$ mG), ambipolar diffusion alters the envelope shapes of the unstable modes, which peak at an intermediate height, instead of being mostly flat as modes in the Hall limit are in this region of parameter space. Similarly, when cosmic rays are assumed to be excluded from the disc by the winds emitted by the magnetically active protostar, unstable modes grow at this radius for $B \lesssim 2$ G. For strong fields, perturbations exhibit a kink at the height where X-ray ionization becomes active. Finally, for $R = 5$ au (10 au), unstable modes exist for $B \lesssim 800$ mG ($B \lesssim 250$ mG) and the maximum growth rate is close to the ideal-MHD rate for $20 \lesssim B \lesssim 500$ mG ($2 \lesssim B \lesssim 50$ mG). Similarly, perturbations incorporating Hall conductivity have a higher wavenumber and grow faster than solutions in the ambipolar diffusion limit for $B \lesssim 100$ mG ($B \lesssim 10$ mG). Unstable modes grow even at the mid-plane for $B \gtrsim 100$ mG ($B \sim 1$ mG), but for weaker fields, a small dead region exists.

This study shows that, despite the low magnetic coupling, the magnetic field is dynamically important for a large range of fluid conditions and field strengths in protostellar discs. An example of such magnetic activity is the generation of MRI unstable modes, which are supported at 1 au for field strengths up to a few gauss. Hall diffusion largely determines the structure and growth rate of these perturbations for all studied radii. At radii of order 1 au, in particular, it is crucial to incorporate the full conductivity tensor in the analysis of this instability and more generally in studies of the dynamics of astrophysical discs.

Key words: accretion, accretion discs – instabilities – MHD – stars: formation.

1 INTRODUCTION

The magnetorotational instability (MRI; Balbus & Hawley 1991, 1998; Hawley & Balbus 1991) generates and sustains angular momentum transport in differentially rotating astrophysical discs. It

[★]Present address: Department of Astronomy & Astrophysics, University of Chicago, 5640 S. Ellis Ave., Chicago, IL 60637, USA.

[†]E-mail: raquel@oddjob.uchicago.edu

does so by converting the free energy source contributed by differential rotation into turbulent motions (e.g. Balbus 2003), which transport angular momentum via Maxwell stresses.

Most MRI models in non-ideal magnetohydrodynamic (MHD) conditions adopt either the ambipolar diffusion (Blaes & Balbus 1994; MacLow et al. 1995; Hawley & Stone 1998) or resistive approximations (Jin 1996; Papaloizou & Terquem 1997; Balbus & Hawley 1998; Sano, Inutsuka & Miyama 1998; Sano & Miyama 1999; Fleming, Stone & Hawley 2000; Sano et al. 2000; Stone & Fleming 2003). The inclusion of Hall diffusion is a relatively recent development (Wardle 1999, W99 hereafter; Balbus & Terquem 2001; Sano & Stone 2002a,b; Salmeron & Wardle 2003, SW03 hereafter; Sano & Stone 2003; Desch 2004). When the Hall effect dominates over ambipolar diffusion, fluid dynamics is dependent on the alignment of the magnetic field with the angular velocity vector of the disc (Wardle & Ng 1999) and wave modes supported by the fluid are intrinsically modified. For example, left- and right-circularly polarized Alfvén waves travel at different speeds and damp at different rates in this regime (Pilipp et al. 1987; Wardle & Ng 1999). Both the structure and growth rate of MRI perturbations can be substantially modified by Hall conductivity, especially when the coupling between ionized and neutral components of the fluid is low (W99; SW03).

In a previous paper, we presented a linear analysis of the vertical structure and growth of the MRI in weakly ionized, stratified accretion discs (SW03). In that study, the components of the conductivity tensor were assumed to be constant with height. The obtained solutions illustrate the properties of the MRI when different conductivity regimes are dominant over the entire cross-section of the disc. We found that when the magnetic coupling is weak, modes computed with a non-zero Hall conductivity grow faster and act over a more extended cross-section than those obtained using the ambipolar diffusion approximation. The height above the mid-plane where the fastest growing modes peak depends on the conductivity regime of the fluid. When ambipolar diffusion is important, perturbations peak at a higher z than when the fluid is in the Hall limit. Furthermore, when the coupling is weak, perturbations computed with a full conductivity tensor peak at different heights depending on the orientation of the magnetic field with respect to the angular velocity vector of the disc. This is a consequence of the dependence of the Hall effect on the sign of $(\mathbf{k} \cdot \boldsymbol{\Omega})(\mathbf{k} \cdot \mathbf{B})$ (Balbus & Terquem 2001), which reduces to $\boldsymbol{\Omega} \cdot \mathbf{B}$ for vertical fields and wavenumbers (W99). Finally, we showed that in the Hall regime perturbations can have a very complex structure (high wavenumber), particularly when the magnetic field is weak. In these conditions, many modes were found to grow, even with a very weak magnetic coupling. These results suggest that significant accretion can occur in regions closer to the mid-plane of astrophysical discs, despite the low magnetic coupling, due to the large column density of the fluid. This idea contrasts with the commonly accepted view that accretion is important primarily in the surface regions, where the coupling between ionized and neutral components of the fluid is much stronger, but the column density is significantly smaller.

In a real disc, the components of the conductivity tensor vary with height (e.g. Wardle 2004) as a result of changes in the abundances of charged particles, fluid density and magnetic field strength. This, in turn, is a consequence of changes in the ionization balance within the disc, which reflects the equilibrium between ionization and recombination processes. The former are primarily non-thermal, triggered by cosmic rays, X-rays emitted by the central protostar and radioactive materials. The latter can, in general, occur both in the gas phase and on grain surfaces (e.g. Oppenheimer & Dalgarno 1974; Spitzer

1978; Umebayashi & Nakano 1980; Nishi, Nakano & Umebayashi 1991; Sano et al. 2000). As a result, different conductivity regimes are expected to dominate at different heights (Wardle 2004). In this paper, we revisit the linear growth and structure of MRI perturbations using a height-dependent conductivity tensor. We assume that the disc is thin and isothermal and adopt a fiducial disc model based on the minimum-mass solar nebula (Hayashi 1981; Hayashi, Nakasawa & Nakagawa 1985). Further, we assume that ions and electrons are the main charge carriers, which is a valid approximation in late stages of accretion, after dust grains have settled towards the mid-plane of the disc. As an indication of the time-scales for this settling to occur, Nakagawa, Nakazawa & Hayashi (1981) show that the mass fraction of $\sim 1\text{--}10\ \mu\text{m}$ grains well mixed with the gas phase, (i.e. not settled), drops from $\sim 10^{-1}$ to 10^{-4} in $t \sim 2 \times 10^3$ to 1×10^5 yr. Furthermore, although the time-scale for dust settling all the way to the equator may exceed the lifetime of the disc, grains can settle within a few pressure scaleheights about the mid-plane in a much shorter time-scale (Dullemond & Dominik 2004).

This paper is structured as follows. Section 2 summarizes the formulation, including the governing equations, fiducial disc model and ionization balance. Section 3 describes the linearization, parameters of the problem and boundary conditions. Results are presented in Sections 4 and 5. We summarize in Section 4 the test models used in this study and present the ionization rates as a function of z at representative radial locations from the central protostar ($R = 1, 5$ and 10 au). The importance of different conductivity regimes at different heights is also described for a range of magnetic field strengths. Then, in Section 5, the structure and growth rate of MRI perturbations at the radii of interest are analysed, including a comparison with results obtained using different configurations of the conductivity tensor, sources of ionization and disc structure. We find that the MRI is active over a wide range of fluid conditions and magnetic field strengths. For example, for the fiducial model at $R = 1$ au and including cosmic ray ionization, unstable modes are found for $B \lesssim 8$ G. When $200\text{ mG} \lesssim B \lesssim 5$ G, these perturbations grow at approximately the ideal-MHD rate ~ 0.75 times the dynamical (Keplerian) frequency of the disc. Results are discussed in Section 6 and the formulation and key findings of the paper are summarized in Section 7.

2 FORMULATION

2.1 Governing equations

Following W99 and references therein, we formulate the conservation equations about a local Keplerian frame corotating with the disc at the Keplerian frequency $\Omega = \sqrt{GM/r^3}$. Time derivatives in this frame, $\partial/\partial t$, correspond to $\partial/\partial t + \Omega\partial/\partial\phi$ in the standard laboratory system (r, ϕ, z) anchored at the central mass M . The fluid velocity is expressed as a departure from Keplerian motion $\mathbf{v} = \mathbf{V} - \mathbf{v}_K$, where \mathbf{V} is the velocity in the laboratory frame and $\mathbf{v}_K = \sqrt{GM/r} \hat{\phi}$ is the Keplerian velocity at the radius r . The fluid is assumed to be weakly ionized, so the effect of ionization and recombination processes on the neutral gas, as well as the inertia and thermal pressure of the ionized species, are negligible. Under this approximation, separate equations of motion for the ionized species are not required and their effect on the neutrals is treated via a conductivity tensor (W99 and references therein), which is a function of location (r, z) .

The governing equations are the continuity equation,

$$\frac{\partial \rho}{\partial t} + \nabla \cdot (\rho \mathbf{v}) = 0, \quad (1)$$

the equation of motion,

$$\frac{\partial \mathbf{v}}{\partial t} + (\mathbf{v} \cdot \nabla) \mathbf{v} - 2\Omega v_\phi \hat{\mathbf{r}} + \frac{1}{2}\Omega v_r \hat{\phi} - \frac{v_K^2}{r} \hat{\mathbf{r}} + \frac{c_s^2}{\rho} \nabla \rho + \nabla \Phi - \frac{\mathbf{J} \times \mathbf{B}}{c\rho} = 0, \quad (2)$$

and the induction equation,

$$\frac{\partial \mathbf{B}}{\partial t} = \nabla \times (\mathbf{v} \times \mathbf{B}) - c \nabla \times \mathbf{E}' - \frac{3}{2}\Omega B_r \hat{\phi}. \quad (3)$$

In the equation of motion (2), Φ is the gravitational potential of the central object, given by

$$\Phi = -\frac{GM}{(r^2 + z^2)^{3/2}}, \quad (4)$$

and v_K^2/r is the centripetal term generated by exact Keplerian motion. Similarly, $2\Omega v_\phi \hat{\mathbf{r}}$ and $\frac{1}{2}\Omega v_r \hat{\phi}$ are the coriolis terms associated with the use of a local Keplerian frame, $c_s = \sqrt{P/\rho}$ is the isothermal sound speed, $\Omega = v_K/r$ is the Keplerian frequency and c is the speed of light. Other symbols have their usual meanings.

In the induction equation (3), \mathbf{E}' is the electric field in the frame comoving with the neutrals and the term $\frac{3}{2}\Omega B_r \hat{\phi}$ accounts for the generation of toroidal field from the radial component due to the differential rotation of the disc.

Additionally, the magnetic field must satisfy the constraint

$$\nabla \cdot \mathbf{B} = 0 \quad (5)$$

and the current density must satisfy Ampère's law,

$$\mathbf{J} = \frac{c}{4\pi} \nabla \times \mathbf{B} \quad (6)$$

and Ohm's law,

$$\mathbf{J} = \sigma \cdot \mathbf{E}' = \sigma_{\parallel} \mathbf{E}'_{\parallel} + \sigma_1 \hat{\mathbf{B}} \times \mathbf{E}'_{\perp} + \sigma_2 \mathbf{E}'_{\perp}. \quad (7)$$

Note that we have introduced the conductivity tensor σ in equation (7). We refer the reader to W99 and references therein for derivations and additional details of this formulation. Assuming that the only charged species are ions and electrons, and that charge neutrality is satisfied ($n_i = n_e$), the components of the conductivity tensor can be expressed as (SW03) the conductivity parallel to the magnetic field,

$$\sigma_{\parallel} = \frac{cen_e}{B} (\beta_i - \beta_e), \quad (8)$$

the Hall conductivity,

$$\sigma_1 = \frac{cen_e}{B} \frac{(\beta_i + \beta_e)(\beta_e - \beta_i)}{(1 + \beta_e^2)(1 + \beta_i^2)}, \quad (9)$$

and the Pedersen conductivity,

$$\sigma_2 = \frac{cen_e}{B} \frac{(1 - \beta_i \beta_e)(\beta_i - \beta_e)}{(1 + \beta_e^2)(1 + \beta_i^2)}. \quad (10)$$

From equations (9) and (10), we find

$$\sigma_{\perp} = \frac{cen_e}{B} \frac{(\beta_i - \beta_e)}{[(1 + \beta_e^2)(1 + \beta_i^2)]^{1/2}}. \quad (11)$$

where $\sigma_{\perp} = \sqrt{\sigma_1^2 + \sigma_2^2}$ is the total conductivity perpendicular to the magnetic field.

In equations (8) to (11),

$$\beta_j = \frac{Z_j e B}{m_j c} \frac{1}{\gamma_j \rho} \quad (12)$$

is the Hall parameter, given by the ratio of the gyrofrequency and the collision frequency of charged species j with the neutrals. It

represents the relative importance of the Lorentz and drag terms in the motion of the charged species. In equation (12),

$$\gamma_j = \frac{\langle \sigma v \rangle_j}{m_j + m}, \quad (13)$$

where m is the mean mass of the neutral particles and $\langle \sigma v \rangle_j$ is the rate coefficient of momentum exchange by collisions with the neutrals. The ion–neutral momentum rate coefficient is given by,

$$\langle \sigma v \rangle_i = 1.6 \times 10^{-9} \text{ cm}^3 \text{ s}^{-1}, \quad (14)$$

an expression that ignores differences in the values of elastic cross-sections of H, H₂ and He (Draine, Roberge & Dalgarno 1983). Similarly, the rate coefficient of momentum exchange of electrons with the neutrals is (Draine et al. 1983)

$$\langle \sigma v \rangle_e \approx 1 \times 10^{-15} \text{ cm}^2 \left(\frac{128kT}{9\pi m_e} \right)^{1/2} \quad (15)$$

and the mean ion mass $m_i = 30 m_H$.

The relative magnitudes of the components of the conductivity tensor differentiate three conductivity regimes: when $\sigma_{\parallel} \gg \sigma_2 \gg |\sigma_1|$ for most charged species, ambipolar diffusion dominates and the magnetic field is effectively frozen into the ionized components of the fluid. Electron–ion drift is small compared with ion–neutral drift and the ionized species act as a single fluid. MRI studies in this regime include Blaes & Balbus (1994), MacLow et al. (1995) and Hawley & Stone (1998). Conversely, when $\sigma_{\parallel} \approx \sigma_2 \gg |\sigma_1|$, the conductivity is a scalar, giving rise to the familiar ohmic diffusion, and the magnetic field is no longer frozen into any fluid component. Examples of studies of the MRI in this regime are Jin (1996), Papaloizou & Terquem (1997), Balbus & Hawley (1998), Sano et al. (1998), Sano & Miyama (1999), Fleming et al. (2000), Sano et al. (2000), Stone & Fleming (2003) and Sano et al. (2004). Ambipolar diffusion dominates in low-density regions, where magnetic stresses are more important than collisions with the neutrals and the ionized species are mainly tied to the magnetic field rather than to the neutral particles. On the contrary, in relatively high density environments, the ionized species are primarily linked to the neutrals via collisions and Ohmic diffusion dominates. There is, however, an intermediate density range characterized by a varying degree of coupling amongst charged species. In these circumstances, there is a component of the conductivity tensor that is perpendicular both to the electric and magnetic fields. It is this term that gives rise to Hall currents. It has been shown that this regime can be important in the weakly ionized environment of accretion discs. For example, using an MRN grain model (Mathis, Rumpl & Nordsieck 1977) with a power-law distribution of grain sizes between 50 and 2500 Å, Wardle & Ng (1999) showed that Hall conductivity is important for $10^7 \lesssim n_H \lesssim 10^{11} \text{ cm}^{-3}$. MRI studies including Hall diffusion have been conducted by W99, Balbus & Terquem (2001), Sano & Stone (2002a,b, 2003), SW03 and Desch (2004).

The ionization balance within the disc (Section 2.3) determines the abundances of charged species (ions and electrons). These, in turn, determine the configuration of the conductivity tensor. In protostellar discs, outside of the central 0.1 au, ionization sources are non-thermal (Hayashi 1981) and the ionization fraction is not enough to produce good magnetic coupling over the entire cross-section of the disc. In these conditions, the region around the mid-plane is likely to be a magnetically ‘dead zone’ (Gammie 1996).

2.2 Disc model

Our model incorporates the vertical structure of the disc, but neglects fluid gradients in the radial direction. This is an appropriate

approximation, as astrophysical accretion discs are generally thin and changes in the radial direction occur on a much bigger length-scale than those in the vertical direction. Including the vertical structure means that perturbations of spatial dimensions comparable to the scaleheight of the disc, which are associated with either a strong magnetic field ($v_A \sim c_s$) or low conductivity, can be explored.

We adopted, as our fiducial model, a disc based on the minimum-mass solar nebula (Hayashi 1981; Hayashi et al. 1985). In this model, the surface density $\Sigma(r)$, sound speed $c_s(r)$, mid-plane density $\rho_0(r)$, scaleheight $H(r)$ and temperature $T(r)$ are:

$$\Sigma(r) = \Sigma_0 \left(\frac{r}{1 \text{ au}} \right)^{-\frac{3}{2}}, \quad (16)$$

$$c_s(r) = c_{s0} \left(\frac{r}{1 \text{ au}} \right)^{-\frac{1}{4}} \left(\frac{L_\star}{L_\odot} \right)^{\frac{1}{8}} \left(\frac{2.34}{\mu} \right)^{\frac{1}{2}}, \quad (17)$$

$$\rho_0(r) = \rho_0 \left(\frac{r}{1 \text{ au}} \right)^{-\frac{11}{4}} \left(\frac{L_\star}{L_\odot} \right)^{-\frac{1}{8}} \left(\frac{M_\star}{M_\odot} \right)^{\frac{1}{2}} \left(\frac{2.34}{\mu} \right)^{\frac{1}{2}}, \quad (18)$$

$$H(r) = H_0 \left(\frac{r}{1 \text{ au}} \right)^{1.25} \quad (19)$$

and

$$T(r) = T_0 \left(\frac{r}{1 \text{ au}} \right)^{-1/2} \left(\frac{L_\star}{L_\odot} \right)^{1/4}. \quad (20)$$

In the previous expressions:

$$\Sigma_0 = 1.7 \times 10^3 \text{ g cm}^{-2}, \quad (21)$$

$$c_{s0} = 9.9 \times 10^4 \text{ cm s}^{-1}, \quad (22)$$

$$\rho_0 = 1.4 \times 10^{-9} \text{ g cm}^{-3}, \quad (23)$$

$$H_0 = 5.0 \times 10^{11} \text{ cm} \quad (24)$$

and

$$T_0 = 280 \text{ K}. \quad (25)$$

In equations (16) to (20), M_\star and L_\star are the stellar mass and luminosity, respectively, and μ is the mean molecular mass of the gas. This model describes the minimum mass distribution of the solar nebula, estimated assuming an efficient planet formation with no significant migration. With these assumptions, the current mass distribution and composition of the planets is a good indication of that of dust in the original nebula. This model has been used extensively, but there are theoretical grounds to expect that a typical protostellar disc may be more massive, with a different large-scale structure, shaped ultimately by the action of MHD turbulence (e.g. Balbus & Papaloizou 1999). Furthermore, disc masses of up to $0.1 M_\odot$, associated with surface density distributions following a power law of index p between 0 and 1, have been derived for T Tauri stars in Taurus (Kitamura et al. 2002). It can be shown that the disc surface density may be roughly up to an order of magnitude higher than the one specified by the minimum-mass solar nebula model before self-gravity becomes important. To account for the possibility of discs being more massive than the minimum-mass solar nebula model, we also studied the properties of MRI unstable modes using a disc structure with an increased surface density $\Sigma'_0 = 10\Sigma_0$ and mass density $\rho'_0 = 10\rho_0$. The Toomre parameter (Toomre 1964) $Q \sim 6$ in this case, so the assumption of a non-self-gravitating disc is still valid.

For simplicity, we assume that the temperature T_0 is unchanged, so H_0 and c_{s0} are the same as in the fiducial model.

As the disc is gravitationally stable, the gravitational force in the vertical direction comes from the central protostar. Under these conditions, the balance between the vertical component of the central gravitational force and the pressure gradient within the disc determines its equilibrium structure. The vertical density distribution of a vertically isothermal disc in hydrostatic equilibrium is given by

$$\frac{\rho(r, z)}{\rho_0(r)} = \exp \left[-\frac{z^2}{2H^2(r)} \right]. \quad (26)$$

Assuming a neutral gas composed of molecular hydrogen and helium such that $n_{\text{He}} = 0.2n_{\text{H}_2}$, the neutral gas mass and number densities are, respectively,

$$\rho = \Sigma n_i m_i = 1.4 m_{\text{H}} n_{\text{H}} \quad (27)$$

and

$$n = 1.2 n_{\text{H}_2}, \quad (28)$$

which gives

$$n_{\text{H}}(r, z) = \frac{\rho(r, z)}{1.4 m_{\text{H}}} \quad (29)$$

and $\mu = \rho/n = 2.34$. For simplicity, we take $L_\star/L_\odot = M_\star/M_\odot = 1$ in all our models.

2.3 Ionization balance

The ionization balance within the disc is given by the equilibrium between ionization and recombination processes. In general, recombination can take place both in the gas phase and on grain surfaces (e.g. Oppenheimer & Dalgarno 1974; Spitzer 1978; Umebayashi & Nakano 1980; Nishi et al. 1991; Sano et al. 2000), but here we have assumed that grains have settled, so we are including only gas-phase recombination rates. Except in the innermost sections of the disc ($R \lesssim 0.1 \text{ au}$), where thermal effects are important (Hayashi 1981), ionization processes in protostellar discs are mainly non-thermal. Ionizing agents are typically cosmic rays, X-rays emitted by the magnetically active protostar, and the decay of radioactive materials present within the disc. Some authors (e.g. Fromang, Terquem & Balbus 2002) have argued that the low-energy particles important for cosmic ray ionization are likely to be excluded by the winds of the protostar. Given the uncertainties involved and the expectation that cosmic rays (if present) may be more important than X-rays near the mid-plane (especially for $R \approx 1 \text{ au}$, where the surface density is larger than the attenuation length of X-rays), we explore both options in this study. The treatment of ionization and recombination processes is detailed below.

2.3.1 Cosmic ray ionization

The cosmic ray ionization rate, $\zeta_{\text{CR}}(r, z)$, is given by,

$$\zeta_{\text{CR}}(r, z) = \frac{\zeta_{\text{CR}}}{2} \left\{ \exp \left[-\frac{\Sigma(r, z)}{\lambda_{\text{CR}}} \right] + \exp \left[-\frac{\Sigma(r) - \Sigma(r, z)}{\lambda_{\text{CR}}} \right] \right\}, \quad (30)$$

where $\zeta_{\text{CR}} = 10^{-17} \text{ s}^{-1}$ is the ionization rate due to cosmic rays in the interstellar medium and $\lambda_{\text{CR}} = 96 \text{ g cm}^{-2}$ is the attenuation length, a measure of how deep cosmic rays can penetrate the disc

(Umebayashi & Nakano 1981). When the surface density is larger than $\sim 2\lambda_{\text{CR}}$, most cosmic rays do not reach the mid-plane. Also,

$$\Sigma(r, z) = \int_z^\infty \rho(r, z) dz \quad (31)$$

is the vertical column density from the location of interest to infinity. The two terms in equation (30) measure the ionization rate at the position (r, z) by cosmic rays penetrating the disc from above and below, respectively.

2.3.2 X-ray ionization

There is strong evidence for an enhanced magnetic activity in young stellar objects (i.e. see review by Glassgold, Feigelson & Montmerle 2000). Typical soft X-ray luminosities (0.2–2 keV) of these objects are in the range of 10^{28} – 10^{30} erg s $^{-1}$, approximately 10^2 – 10^3 times more energetic than solar levels (Glassgold et al. 2000). Models of the penetration of stellar X-rays into a protostellar disc by Igea & Glassgold (1999) show that, even discounting the low-energy photons that are attenuated by stellar winds, the ionization rate due to hard X-rays close to the central object is many orders of magnitude larger than that of cosmic rays, especially above $z/H \sim 2$. These authors investigated the ionization rate by X-rays from a central protostar modelled as an X-ray source of total luminosity $L_X \sim 10^{29}$ erg s $^{-1}$ and temperature kT_X in the range of 3–8 keV. The transport of X-rays through the disc was followed using a Monte Carlo procedure, which included both absorption and scattering by disc material. The incorporation of scattering is important, as X-rays can be scattered not only out of the disc, but also towards the mid-plane, enhancing the ionization level deeper within the disc. Results indicate that, at each radius, the X-ray ionization rate is a function of the vertical column density into the disc $N_\perp(r, z)$, irrespective of its structural details.

To calculate the X-ray ionization rate $\zeta_X(r, z)$ in the upper half of the disc, we added the contribution of X-rays arriving from both sides. We used the values of $\zeta_X(r, z)$ (s $^{-1}$) as a function of the vertical column density, N_\perp (cm $^{-2}$), plotted in fig. 3 of Igea & Glassgold (1999), for $R = 1, 5$ and 10 au and $kT_X = 5$ keV. The vertical column density, appropriate for X-rays arriving from the top, is

$$N_\perp(r, z) = \int_z^\infty n_H(r, z) dz, \quad (32)$$

with n_H given by equation (29). Similarly, the ionization contributed by X-rays arriving at $(r, z > 0)$ from the other hemisphere of the disc is obtained substituting N_\perp above by $2N_\perp(r, 0) - N_\perp(r, z)$, although this contribution is usually negligible.

2.3.3 Radioactivity

The ionization rate ζ_R contributed by the decay of radioactive materials (primarily ^{40}K) have also been considered in previous work (i.e. Consolmagno & Jokipii 1978; Sano et al. 2000). This rate can be calculated as (Consolmagno & Jokipii 1978)

$$\zeta_R = \frac{\gamma n_r E}{\Delta \varepsilon}, \quad (33)$$

where γ (s $^{-1}$) is the decay rate of the radioactive isotopes, n_r their number density relative to hydrogen and E (eV) the energy of the produced radiation. Similarly, $\Delta \varepsilon = 37$ eV is the average energy for the production of an ion pair in H_2 gas (Consolmagno & Jokipii 1978 and references therein; Shull & Van Steenberg 1985; Voit 1991). In the present study, we have adopted

$$\zeta_R = 6.9 \times 10^{-23} [\delta_2 + (1 - \delta_2) f_g] \text{ s}^{-1} \quad (34)$$

(Umebayashi & Nakano 1981, 1990). Here, $\delta_2 \approx 0.02$ is the fraction of heavy metal atoms in the gas phase, estimated via measurements of interstellar absorption lines in diffuse clouds (Morton 1974). It is, of course, possible that δ_2 in discs could be even smaller than this value. On the other hand, f_g is a parameter that takes into account the degree of sedimentation of dust grains in protostellar discs with respect to interstellar values (Hayashi 1981; Sano et al. 2000).

Although the ionization effect contributed by this agent is very small compared with that of X-rays and cosmic rays, we included it because it may well be the only mechanism active in regions close to the mid-plane (particularly for $R \lesssim 5$ au) in the scenario where cosmic rays are excluded from the disc. In this case, it is important to explore the sensitivity of MRI perturbations to changes in the level of depletion of dust grains (f_g).

We have assumed here that the ionized component of the fluid is made of ions and electrons only, a case that corresponds to late evolutionary stages of protostellar discs, after dust grains have settled towards the mid-plane. Accordingly, we assume $f_g = 0$ in all our models, except when specifically exploring the role of radioactivity in a disc where cosmic rays are assumed to be excluded from it.

2.3.4 Recombination rate

Gas-phase recombination occurs through dissociative recombination of electrons with molecular ions and, at a slower rate, via radiative recombination with metal ions. It has been pointed out by previous authors that the ionization balance may be especially sensitive to the presence of metal atoms within the disc. For some disc configurations, a number density of metals as small as 10^{-7} times the cosmic abundance may be enough to make the whole cross-section of the disc turbulent, eliminating the central magnetic dead zone (Fromang et al. 2002). This is so because metal atoms generally take the charges of molecular ions, but recombine with electrons (via radiative processes) at a much slower rate.

If n_m^+ and n_m^+ are the number densities of molecular and metal ions, respectively, the rate equations for n_e and n_m^+ can be expressed as (e.g. Fromang et al. 2002):

$$\frac{dn_e}{dt} = \zeta n_H - \beta n_e n_m^+ - \beta_r n_e n_M^+ \quad (35)$$

and

$$\frac{dn_m^+}{dt} = \zeta n_H - \beta n_e n_m^+ - \beta_r n_m n_M^+, \quad (36)$$

where ζ is the total ionization rate, calculated as summarized in the previous sections, and n_H is the hydrogen number density from equation (29). From equations (35) and (36), it follows that, in equilibrium,

$$\beta_r n_e n_M^+ = \beta n_m n_M^+. \quad (37)$$

In the previous expressions, β is the dissociative recombination rate coefficient for molecular ions, β_r is the radiative recombination rate coefficient for metal ions and β_i is the rate coefficient of charge transfer from molecular ions to metal atoms. If it is assumed that all metals are locked into dust grains, which have in turn sedimented towards the mid-plane of the disc (i.e. $n_M \approx 0$), equations (35) and (36), together with charge neutrality, $n_e = n_m^+ + n_M^+$, and appropriate values for the rate coefficients,

$$\beta_r = 3 \times 10^{-11} T^{-1/2} \text{ cm}^3 \text{ s}^{-1}, \quad (38)$$

$$\beta = 3 \times 10^{-6} T^{-1/2} \text{ cm}^3 \text{ s}^{-1}, \quad (39)$$

$$\beta_l = 3 \times 10^{-9} \text{cm}^3 \text{s}^{-1} \quad (40)$$

(see Fromang et al. 2002 and references therein), lead to

$$n_e \approx \sqrt{\frac{\zeta n_H}{\beta}}. \quad (41)$$

However, as these authors point out also, dust grains not only absorb metal atoms, but also release them as a result of the action of X-rays. Because of this effect, the abundance of metal atoms in a disc could be quite insensitive to the spatial distribution of dust grains. This, in turn, means that dust settling does not necessarily lead to a severe reduction in the number density of metal atoms in the gas phase. If these dominate, the corresponding n_e is

$$n_e \approx \sqrt{\frac{\zeta n_H}{\beta_r}}. \quad (42)$$

The transition from one regime to the other is taken here to occur when x_M is such that $\beta_r n_e n_M^+ > \beta n_e n_m^+$. When this condition is satisfied, electrons are more likely to recombine radiatively with metal ions than they are to recombine dissociatively with molecular ions (see equation 35). Using equation (37), this leads to

$$x_M > \frac{\beta}{\beta_l} x_e = 10^3 T^{-1/2} x_e. \quad (43)$$

Note that this minimum x_M for radiative recombination to dominate is more stringent (by 5 orders of magnitude) than the expression given by Fromang et al. (2002). These authors identified the transition with $x_M \approx x_m^+$ and obtained $x_M > 10^{-2} T^{-1/2} x_e$ for metals to be dominant. However, given that $\beta_r \ll \beta$, when this condition is satisfied electrons will still be more likely to recombine with molecular ions. As a result, in this study we have adopted expression (43) as the minimum x_M for radiative recombination to dominate. The electron number density n_e and, hence, the magnetic coupling χ (see Section 3.2) in the limit where dissociative recombination dominates (equation 41) are $\sqrt{\beta_r/\beta} \sim 300$ times lower than the one obtained in the metal-dominated limit (equation 42). However, the former recombination mechanism dominates when $\beta_r n_e n_M^+ < \beta n_e n_m^+$, which gives a maximum x_M given by expression (43) with the appropriate x_e for this limit (equation 41). This metal abundance is, similarly, a factor of ~ 300 lower than the minimum abundance for radiative dominance. As a result, the transition between these two regimes is not instantaneous: it occurs over a range of x_M . The full reduction in n_e (and χ) is only realized when x_M is a factor of ~ 300 below the critical value of equation (43). For the fiducial model this occurs 1.5 scaleheights above the location indicated by this expression. Finally, if X-rays are able to liberate metal atoms from dust grains and the metal abundance becomes fairly independent of the dust spatial distribution (Fromang et al. 2002), then the actual x_M can be up to a factor of $1/\delta_2$ larger than the value adopted in this work (see Section 4.2). If this is the case, the transition (from radiative to dissociative recombination regimes) will take place even higher above the mid-plane.

From the previous discussion, it is clear that the evolutionary stage and activity of the disc are important factors in the ionization balance, as they influence the degree of sedimentation of dust grains. As the disc evolves, dust grains tend to occupy a thin layer around the mid-plane, becoming removed (in any dynamical sense) from the gas at higher vertical locations. This causes the ionization fraction of the gas to increase, by eliminating recombination pathways on dust surfaces. In the present work, we have used equation (42) to calculate the electron (and ion) number density. The minimum values of x_M for this approximation to be valid (equation 43) have also been

computed and compared with an estimate of metal abundances in the gas phase (see Section 4.2). Results indicate that, for the range of parameters adopted here, the abundance of metal atoms is such that radiative recombination is indeed dominant, except in the upper regions of the disc, so the use of equation (42) to calculate the electron fraction is justified.

3 METHODOLOGY

3.1 Linearization

Full details of the methodology are described in SW03. For the sake of clarity and completeness, we summarize here the most important steps and point at some differences with the previous formulation. The system of equations (1) to (3), (6) and (7) was linearized about an initial steady state where fluid motion is exactly Keplerian and the magnetic field is vertical, so $\mathbf{J} = \mathbf{v} = \mathbf{E}' = 0$ and $\mathbf{B} = B\hat{z}$. In the initial state both \mathbf{E}' and \mathbf{J} vanish, so the changes in the conductivity tensor due to the perturbations do not appear in the linearized equations. As a result, it is not necessary to explore how the perturbations affect the conductivity of the fluid and only the values in the initial steady state are required.

We assume that the wavevector of the perturbations is perpendicular to the plane of the disc ($k = k_z$). These perturbations, initiated from a vertical magnetic field, are the fastest growing modes when the fluid is in either the Hall or resistive conductivity regimes, as in these cases magnetic pressure suppresses displacements with a non-zero radial wavenumber (Balbus & Hawley 1991; Sano & Miyama 1999). However, as pointed out by Desch (2004) and Kunz & Balbus (2004), this is not necessarily the case for perturbations in the ambipolar diffusion limit. The results of these studies indicate that in this regime, the fastest growing modes may exhibit both radial and vertical wavenumbers.

Taking perturbations of the form $\mathbf{q} = \mathbf{q}_0 + \delta\mathbf{q}(z)e^{i\omega t}$ about the initial state, linearizing and neglecting terms of order H/r or smaller, we find that the final linear system of equations that describes the MHD perturbations within the disc is:

$$i\omega\rho\delta v_r - 2\rho\Omega\delta v_\phi - \frac{B_0}{c}\delta J_\phi = 0, \quad (44)$$

$$i\omega\rho\delta v_\phi + \frac{1}{2}\rho\Omega\delta v_r + \frac{B_0}{c}\delta J_r = 0, \quad (45)$$

$$i\omega\delta B_r - c\frac{d\delta E_\phi}{dz} = 0, \quad (46)$$

$$i\omega\delta B_\phi + c\frac{d\delta E_r}{dz} + \frac{3}{2}\Omega\delta B_r = 0, \quad (47)$$

$$\delta J_r = -\frac{c}{4\pi}\frac{d\delta B_\phi}{dz}, \quad (48)$$

$$\delta J_\phi = \frac{c}{4\pi}\frac{d\delta B_r}{dz}, \quad (49)$$

$$\delta J_r = \sigma_2\delta E'_r - \sigma_1\delta E'_\phi, \quad (50)$$

$$\delta J_\phi = \sigma_1\delta E'_r + \sigma_2\delta E'_\phi, \quad (51)$$

where δE_ϕ and δE_r are the perturbations of the electric field in the laboratory frame,

$$\delta E_\phi = \delta E'_\phi + \frac{B_0}{c}\delta v_r, \quad \text{and} \quad (52)$$

$$\delta E_r = \delta E'_r - \frac{B_0}{c}\delta v_\phi. \quad (53)$$

Note that σ_{\parallel} , the component of the conductivity tensor parallel to the magnetic field, does not appear in the linearized equations. This, in turn, implies that in the linear phase of the MRI and under the adopted approximations, the ambipolar diffusion and resistive conductivity regimes behave identically (see Section 2.1).

We express equations (44) to (53) in dimensionless form by normalizing the variables as follows:

$$\begin{aligned} z^* &= \frac{z}{H}, & \rho^* &= \frac{\rho(r, z)}{\rho_0(r)}, & \delta \mathbf{B}^* &= \frac{\delta \mathbf{B}}{B_0}, \\ \delta \mathbf{v}^* &= \frac{\delta \mathbf{v}}{c_s}, & \delta \mathbf{E}^* &= \frac{c \delta \mathbf{E}}{c_s B_0}, & \delta \mathbf{E}'^* &= \frac{c \delta \mathbf{E}'}{c_s B_0}, \\ \delta \mathbf{J}^* &= \frac{c \delta \mathbf{J}}{c_s B_0 \sigma_{\perp}}, & \sigma^* &= \frac{\sigma}{\sigma_{\perp}}. \end{aligned}$$

Here, subscript ‘o’ denotes variables at the mid-plane of the disc. Note that we have used the local σ_{\perp} instead of $\sigma_{\perp 0}$, used in SW03, to normalize σ and $\delta \mathbf{J}$. This is more useful when dealing with a height-dependent conductivity. In the following dimensionless system, we have dropped the asterisks and expressed the final equations in matrix form:

$$\frac{d}{dz} \begin{pmatrix} B_r \\ B_{\phi} \\ E_r \\ E_{\phi} \end{pmatrix} = \begin{pmatrix} 0 & 0 & C_1 A_1 & C_1 A_2 \\ 0 & 0 & -C_1 A_2 & C_1 A_3 \\ -\frac{3}{2} & -\nu & 0 & 0 \\ \nu & 0 & 0 & 0 \end{pmatrix} \begin{pmatrix} B_r \\ B_{\phi} \\ E_r \\ E_{\phi} \end{pmatrix}, \quad (54)$$

$$\delta \mathbf{J} = C_2 \begin{pmatrix} A_2 & -A_3 \\ A_1 & A_2 \end{pmatrix} \delta \mathbf{E}, \quad (55)$$

$$\delta \mathbf{v} = \chi \frac{1}{1 + \nu^2} \begin{pmatrix} -2 & \nu \\ -\nu & -\frac{1}{2} \end{pmatrix} \delta \mathbf{J}, \quad (56)$$

$$\delta \mathbf{E}' = \frac{1}{\sigma_{\perp}} \begin{pmatrix} \sigma_2 & \sigma_1 \\ -\sigma_1 & \sigma_2 \end{pmatrix} \delta \mathbf{J}, \quad (57)$$

where

$$\nu = \frac{i\omega}{\Omega}, \quad (58)$$

$$C_1 = \chi \left(\frac{v_A}{c_s} \right)^{-2} C_2, \quad (59)$$

$$C_2 = \left[1 + \chi \frac{1}{1 + \nu^2} \left(\frac{5}{2} \frac{\sigma_1}{\sigma_{\perp}} + 2\nu \frac{\sigma_2}{\sigma_{\perp}} + \chi \right) \right]^{-1}, \quad (60)$$

$$A_1 = \frac{\sigma_1}{\sigma_{\perp}} + 2\chi \frac{1}{1 + \nu^2}, \quad (61)$$

$$A_2 = \frac{\sigma_2}{\sigma_{\perp}} + \nu \chi \frac{1}{1 + \nu^2} \quad \text{and} \quad (62)$$

$$A_3 = \frac{\sigma_1}{\sigma_{\perp}} + \frac{1}{2} \chi \frac{1}{1 + \nu^2}. \quad (63)$$

In the above expressions,

$$v_A = \frac{B_0}{\sqrt{4\pi\rho}} \quad (64)$$

is the local Alfvén speed in the disc and

$$\chi \equiv \frac{\omega_c}{\Omega} \equiv \frac{1}{\Omega} \frac{B_0^2 \sigma_{\perp}}{\rho c^2} \quad (65)$$

controls the local coupling between the magnetic field and the disc (W99; SW03; see also Section 3.2). Non-ideal effects strongly modify wavemodes at, or above, the critical frequency ω_c .

3.2 Parameters

The following parameters control the dynamics and evolution of the fluid.

(i) v_A/c_s , the ratio of the local Alfvén speed to the isothermal sound speed of the gas. It is a measure of the strength of the magnetic field. In ideal-MHD conditions, unstable modes grow when the magnetic field is subthermal ($v_A/c_s < 1$). Under this approximation, when $v_A \sim c_s$ the minimum wavelength of the instability is of the order of the scaleheight of the disc and the growth rate decreases rapidly. This is also the case under the assumption that ambipolar or ohmic diffusion dominates over the entire cross-section of the disc (SW03). However, when the fluid is in the Hall regime, with the magnetic field counteraligned with the angular velocity vector of the disc ($\Omega \cdot \mathbf{B} < 0$), MRI unstable modes may exist for stronger fields, up to $v_A/c_s \sim 3$ (SW03).

(ii) χ , a parameter that characterizes the strength of the local coupling between the magnetic field and the disc (equation 65). It is given by the ratio of the critical frequency above which flux-freezing conditions break down and the dynamical (Keplerian) frequency of the disc. If $\chi \equiv \omega_c/\Omega < 1$, the disc is poorly coupled to the disc at the frequencies of interest for dynamical analysis, which are also the interesting frequencies for the study of the MRI.

(iii) σ_1/σ_2 , the ratio of the conductivity terms perpendicular to the magnetic field. It is an indication of the conductivity regime of the fluid, as discussed in Section 2.1.

We calculated the values of the three parameters above at different locations (r, z) within the disc using equations (9), (10), (17), (64) and (65). The strength of the magnetic field is a free parameter: we consider field strengths in excess of 1 mG.

3.3 Boundary conditions

To solve equations (54) to (57), it is necessary first to integrate the system of ordinary differential equations (ODE) in equation (54). This can be treated as a two-point boundary value problem for coupled ODE. Five boundary conditions must be formulated, prescribed either at the mid-plane or at the surface of the disc.

(i) At the mid-plane: we chose to assign odd symmetry to δB_r and δB_{ϕ} , so they vanish at $z = 0$. This gives us two boundary conditions at the mid-plane. Also, as the equations are linear, their overall scaling is arbitrary and a third boundary condition can be obtained by setting one of the fluid variables to any convenient value. To that effect, we assigned a value of 1 to $\delta E'_r$. The three boundary conditions applied at the mid-plane are then

$$\begin{aligned} \delta B_r &= \delta B_{\phi} = 0 \quad \text{and} \\ \delta E'_r &= 1. \end{aligned}$$

(ii) At the surface: χ is inversely proportional to the density (equation 65), so if the conductivity is assumed to be constant with height, it increases monotonically with z . This was the case in SW03, where we used this argument to propose that, at sufficiently high z above the mid-plane, ideal MHD conditions held. This, in turn, implies that the wavelengths of magnetic field perturbations, given the

adopted dependence of ρ on z (equation 26), must tend to infinity when $z \rightarrow \infty$. As a result, the amplitude of such modes should vanish at infinity as well. Here, however, the conductivities vary with z , so this argument needs revisiting. In Section 4.3, we analyse the dependence of χ with height for different radial positions and a range of magnetic field strengths. Here, we just highlight that at the surface of the disc ($z/H = 6$, see below), the magnetic coupling is still strong. For example, for the fiducial model at $R = 1$ au, $\chi \sim 20$. It decreases to ~ 4.5 for $R = 5$ au and to ~ 2.5 for $R = 10$ au. This is still above the limit (~ 1) for strong coupling (W99).

When $\chi > 10$, the growth rate and characteristic wavenumber of local unstable modes differ little from the ideal limit (W99), so the same line of reasoning of SW03 can be used to argue that in this case δB_r and δB_ϕ should be zero at the boundary as well. Although χ at the surface when $R \gtrsim 5$ au is below 10, it is considered that the magnetic coupling there is still sufficiently strong for the ideal-MHD approximation to be essentially valid as well. This is also confirmed by the way in which magnetic field perturbations tend to zero at the boundary at these radii (see results in Sections 4 and 5). Consistently with this, both $\delta \mathbf{E}'$ and $\delta \mathbf{J}$ vanish at the surface as well. This gives us the remaining two boundary conditions required to integrate the system of equations (54). Gammie & Balbus (1994) obtained similar boundary conditions for their ‘hot halo model’, where the disc is terminated in a hot, perfectly conducting halo at a height z_h above the midplane. These authors showed that the perturbed magnetic field in this halo is approximately force-free, so $(\nabla \times \delta \mathbf{B}) \times \mathbf{B}_0 \approx 0$, and $\nabla \times \delta \mathbf{B} = a \mathbf{B}_0$. In the last expression, ‘ a ’ is a function that is constant along the unperturbed field lines. For vanishing stress at infinity (the condition we are adopting here) $a \equiv 0$, which recovers the conditions $\delta B_r = \delta B_\phi = 0$ at the surface of the disc.

We chose to locate the boundary at $z/H = 6$, after confirming that increasing this height does not significantly affect either the structure or the growth rate of unstable modes. Summarizing, the boundary conditions adopted at the surface are

$$\delta B_r = \delta B_\phi = 0$$

at $z/H = 6$.

This system of equations is solved by ‘shooting’ from the mid-plane to the surface of the disc while simultaneously adjusting the growth rate ν and $\delta E'_\phi$ at the mid-plane. The adjustment is done via a multidimensional, globally convergent Newton–Raphson method, until the solution converges. The procedure involves supplying initial guessed values for these two variables to start the iteration. In order to avoid missing an unstable mode – in particular, the fastest growing mode – we successively tried guessed values of ν_{\max} in the range of 0.1 to 1.0, in intervals of 0.01. Given that $\nu_{\max} < 0.75$ (BH91) we are confident that the most unstable mode is not missed, even though it can not be guaranteed that all modes are always found.

4 DISC CONDUCTIVITY

4.1 Test models

Our fiducial model is based on the solar nebula disc (Hayashi 1981; Hayashi, Nakazawa & Nakagawa 1985; see Section 2.2). The structure and growth rate of MRI unstable modes are calculated at representative radial positions ($R = 1, 5$ and 10 au) from the central protostar. Two scenarios are explored: cosmic rays either penetrate the disc, although attenuated as appropriate (as given by equation 30), or they are excluded from it by the winds produced by the central

object. Unless stated otherwise, results presented using this model include cosmic ray ionization. We also consider a disc model with an increased mass and surface density, as described in Section 2.2. For simplicity, other disc parameters remain unchanged and, in this case, all calculations incorporate the ionization rate provided by cosmic rays.

We also compare solutions obtained using different configurations of the conductivity tensor. By comparing the structure and growth rate of unstable modes found using the commonly adopted ambipolar diffusion (or resistive; $\sigma_1 = 0$) approximations with those obtained with a full conductivity tensor ($\sigma_1 B_z > 0, \sigma_2 \neq 0$), as well as the less common Hall limit ($\sigma_2 = 0, \sigma_1 B_z > 0$), we can appreciate how and in which regions of parameter space Hall conductivity alters the properties of the instability. This is explored for the fiducial model at 1 au only.

The properties of the MRI in the Hall limit are dependent on the alignment of the magnetic field and angular velocity vectors of the disc (W99). The case when these vectors are parallel (antiparallel) is characterized by $\sigma_1 B_z > 0$ ($\sigma_1 B_z < 0$). In the Hall ($\sigma_1 B_z < 0$) limit, our code fails to converge whenever the combination of parameters is such that $\chi < 2$ anywhere in the domain of integration. This is not surprising as, in this regime, when $0.5 < \chi < 2$ all wavenumbers are unstable (W99). As a result, we explored the effect of the alignment of \mathbf{B} and $\boldsymbol{\Omega}$ by comparing solutions obtained with a full conductivity tensor but incorporating $\sigma_1 B_z$ terms of opposite sign. Even with this approach, solutions including a $\sigma_1 B_z < 0$ term could not be computed at all for $R = 1$ au, given that the mid-plane coupling at this radius is extremely low ($\sim 10^{-10}$ to 10^{-2} for B between 1 mG and 1 G). Therefore, we present this analysis at 5 and 10 au only. Solutions incorporating a negative Hall conductivity could be obtained for $B \gtrsim 8$ mG at 5 au and $B \gtrsim 1.5$ mG at 10 au, where the magnetic coupling at the mid-plane is $\gtrsim 2$.

Unless stated otherwise, results discussed in the following sections incorporate a $\sigma_1 B_z > 0$ Hall term contribution.

4.2 Ionization rates

Fig. 1 shows the ionization rate contributed by cosmic rays, X-rays and radioactive materials as a function of height for the fiducial model. Results are presented at the radial locations of interest: 1, 5 and 10 au. Note that X-rays penetrate up to $z/H \sim 1.7$ and $z/H \sim 0.3$ for $R = 1$ and 5 au, respectively. They reach the mid-plane for $R = 10$ au. The X-ray ionization rate is heavily attenuated below ~ 1.5 to 2 scaleheights from the surface, depending on the radius.

At 1 and 5 au, the regions where X-rays are not able to penetrate are ionized only by the action of cosmic rays (if present) and radioactive decay. Moreover, cosmic rays constitute the most efficient ionizing agent for $z/H \lesssim 2.2$ at all studied radii. As a result, if they are excluded from the disc by the winds of the protostar (i.e. Fromang et al. 2002), the magnetic coupling of the gas in these sections of the disc is expected to be severely reduced. In order to explore the properties of MRI perturbations under this assumption, we compare results computed including and excluding this source of ionization for the fiducial model (Sections 5.1.2 and 5.1.3, respectively).

Igea & Glassgold (1999) have pointed out that, in protostellar discs, the X-ray ionization rate can be 10^3 – 10^5 times that of interstellar cosmic rays. Their calculations show that X-rays dominate over cosmic rays until the vertical column density, N_\perp , is 10^{25} , 5×10^{23} and $2 \times 10^{23} \text{ cm}^{-2}$ for $R = 1, 5$ and 10 au, respectively. Once N_\perp exceeds $\sim 10^{25} \text{ cm}^{-2}$, X-ray ionization dies out because there are no remaining incident photons available. The ionization rates adopted in this study (Fig. 1) are in agreement with these findings.

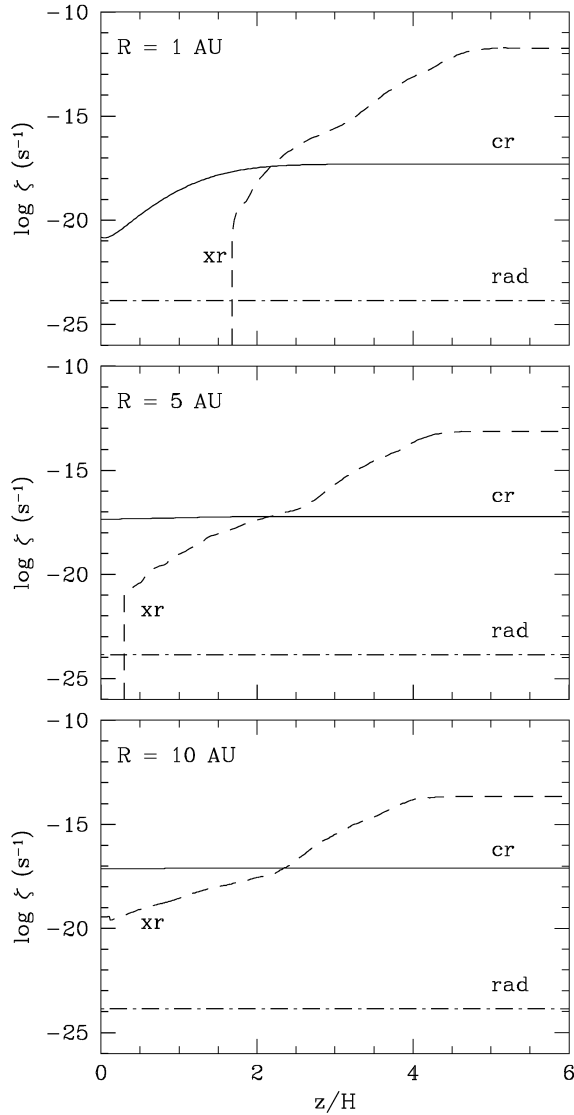


Figure 1. Ionization rate (s^{-1}) contributed by cosmic rays (curve labelled ‘cr’), X-rays (xr) and radioactive materials (rad) as a function of height, for the fiducial model (minimum-mass solar nebula disc). Results are shown for $R = 1, 5$ and 10 au. Note that, at 1 au, cosmic ray ionization is attenuated with respect to the interstellar rate for $z/H \lesssim 2$. Also, X-rays are excluded from the disc for $z/H \lesssim 1.7$ (at 1 au) and $z/H \lesssim 0.3$ (at 5 au). For $R = 10$ au, they reach the mid-plane, although their ionization rate is heavily attenuated. Cosmic rays (if present) are the most efficient ionizing agent for $z/H \lesssim 2.2$ in all cases.

We have used equation (42) to calculate the electron number density (Section 2.3.4). This expression is valid when metal atoms dominate and electrons recombine primarily via radiative processes. Here, we justify this choice. Fig. 2 compares the minimum abundance of metals (equation 43) for this approximation to be valid with an estimate of total metal abundances in the gas phase. Minimum abundances (relative to hydrogen) are shown for the radial locations of interest for the fiducial model. The total gas-phase metal abundance is taken as $8.4 \times 10^{-5} \delta_2$ (Umebayashi & Nakano 1990). From Fig. 2, it is clear that the abundance of gas-phase metal atoms is expected to exceed the minimum for radiative recombination processes to be dominant at all radii of interest here, except in the upper sections of the disc (i.e. $z/H \lesssim 3.5$ at 1 au). Given that the fastest growing MRI modes are strongly damped in these regions

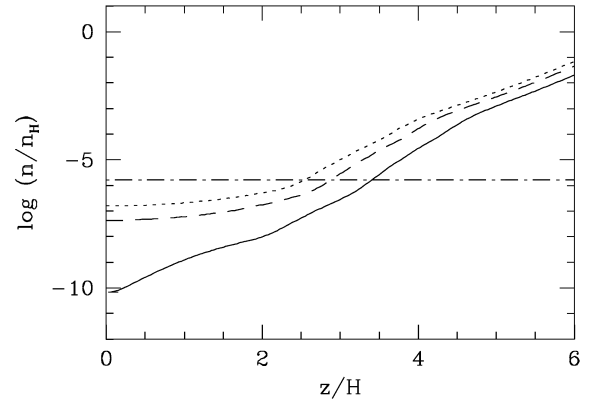


Figure 2. Comparison of the minimum abundance of metal atoms in the gas phase, $x_M = n_M/n_H$, for the radiative recombination rate of metal ions (β_r) to be the dominant recombination mechanism, and an estimate of the total gas-phase metal abundance, as a function of height. Minimum abundances are shown for the fiducial model at 1 au (solid line), 5 au (dashed line) and 10 au (dotted line). The estimated total gas-phase metal abundance (dot-dashed line) is from Umebayashi & Nakano (1990). This abundance exceeds the minimum required for all radii and vertical locations of interest in this study, except in the upper sections of the disc. This is not expected to significantly affect the results presented in this study, given that the fastest growing MRI modes are strongly damped in these regions.

(see Fig. 9, later) and that the full impact on n_e (and χ) when dissociative recombination dominates is not achieved until x_M is a factor of ~ 300 below the critical value of equation (43) (see Section 2.3.4), we conclude that equation (42) is still a valid approximation to calculate the electron number density in this study.

4.3 Magnetic coupling and conductivity regimes as a function of height

It is interesting to explore which conductivity terms (Section 2.1) are dominant at different heights at the representative radial locations we are considering. This information will be used in the analysis of the structure and growth of MRI unstable modes in the next section. We recall that Hall diffusion is locally dominant when (SW03)

$$\chi < \chi_{\text{crit}} \equiv \frac{|\sigma_1|}{\sigma_{\perp}}. \quad (66)$$

When χ is higher than this, but still $\lesssim 10$, ambipolar diffusion dominates. In regions where χ is stronger, ideal-MHD conditions hold (W99). We remind the reader that, in the present formulation, the ambipolar and Ohmic conductivity regimes behave identically. This is the case because σ_{\parallel} (the conductivity component that distinguishes between them) does not appear in the final, linearized system of equations (see Section 3.1). This should be kept in mind when analysing the results, as even though the case where $\sigma_1 = 0$ has been referred to as the ‘ambipolar diffusion’ limit ($\sigma_{\parallel} \gg \sigma_2$), it is also consistent with the ‘resistive’ regime ($\sigma_{\parallel} \sim \sigma_2$).

We are interested in comparing χ and χ_{crit} as a function of height for different disc models, radial locations and choices of the magnetic field strength. An example of the typical dependence of these variables on z is shown in Fig. 3 for the fiducial model at $R = 1$ au for $B = 10$ mG. Note that the conductivity term parallel to the field increases monotonically with z and is independent of B (see equations 8 and 12). In this case, $|\sigma_1|$ is nearly 2 orders of magnitude smaller than σ_2 at the mid-plane. As a result, near the mid-plane $\sigma_{\parallel} \sim \sigma_2 \gg |\sigma_1|$ and the fluid is in the resistive regime (Section 2.1). This is consistent with findings by Wardle (in preparation) that

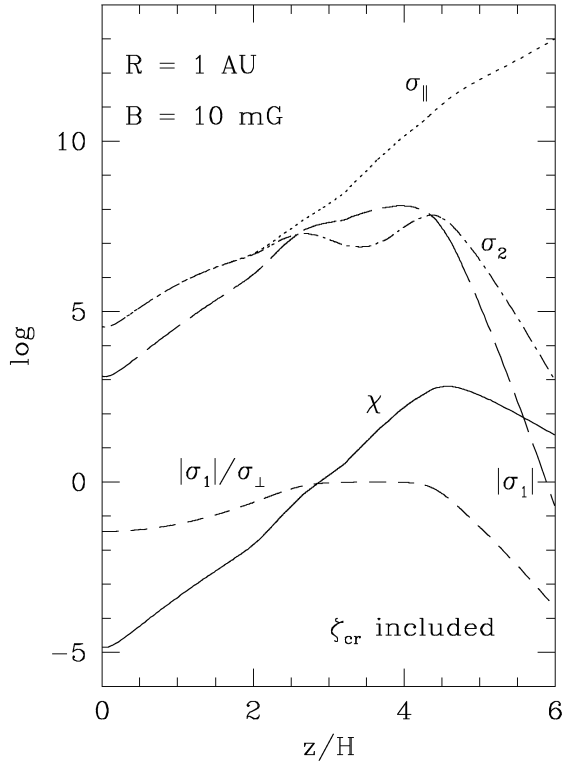


Figure 3. Example of the dependence of the conductivity components parallel (σ_{\parallel}) and perpendicular ($|\sigma_1|$ and σ_2) to the field, magnetic coupling (χ) and $\chi_{\text{crit}} \equiv |\sigma_1|/\sigma_{\perp}$ as a function of height. Results shown correspond to the fiducial model for $R = 1$ au and $B = 10$ mG. Note that for $z/H \lesssim 2$, $\sigma_{\parallel} \sim \sigma_2 \gg |\sigma_1|$ and the conductivity is resistive. There is then a central section for which $|\sigma_1| \gg \sigma_2$ (the fluid is in the Hall conductivity regime), while for higher vertical locations $\sigma_{\parallel} \gg \sigma_2 \gg |\sigma_1|$ and ambipolar diffusion dominates. In the region where $\chi < \chi_{\text{crit}}$, Hall diffusion dominates the structure and growth rate of the MRI (SW03). Note also that χ could be reduced by up to a factor of 300 near the surface if dissociative (and not radiative) recombination dominates the ionization balance at high z above the mid-plane.

Ohmic conductivity is important at this radius for relatively weak fields ($B \lesssim 100$ mG) when the density is sufficiently high (e.g. $n_{\text{H}} \gtrsim 10^{12} \text{ cm}^{-3}$ for $B = 1$ mG). Both components of the conductivity tensor perpendicular to the field increase with height initially, reflecting the enhanced ionization fraction at higher z . There is then a central section of the disc where $|\sigma_1| \gg \sigma_2$ (the fluid is in the Hall regime) and, finally, both terms drop abruptly closer to the surface as a consequence of the fall in fluid density. Note that the Hall conductivity term decreases much more sharply than the ambipolar diffusion component. As a result, the ambipolar diffusion term is typically several orders of magnitude greater than the Hall term in the surface regions of the disc. To reiterate this concept, we repeat here that, even in regions where $|\sigma_1| \ll \sigma_2$, the growth and structure of the MRI in the linear regime are still dominated by Hall diffusion if $\chi \lesssim |\sigma_1|/\sigma_{\perp}$ (SW03).

The previous results are in agreement with the notion that $|\sigma_1| > \sigma_2$ at intermediate heights, where $|\beta_e| \gg 1$ while $\beta_i \ll 1$. At higher z , typically $|\beta_e| \gg \beta_i \gg 1$ and the fluid is in the ambipolar diffusion regime. In these conditions, equations (9) and (10) show that $|\sigma_1| \ll \sigma_2$. On the contrary, near the mid-plane either component may dominate, depending on the fluid density and the strength of the magnetic field. $|\sigma_1|$ will be larger if the fluid density is relatively small (larger radius) and/or the field is stronger. Conversely, if the

field is weak and the density is sufficiently high, $\sigma_{\parallel} \sim \sigma_2 \gg |\sigma_1|$ and the conductivity will be resistive. This behaviour of the conductivity components as a function of height explains, in turn, the dependence of χ_{crit} on z : for weak fields, it is $\ll 1$ near the mid-plane ($\sigma_2 \gg |\sigma_1|$), but if B is sufficiently strong, χ_{crit} close to the mid-plane is ~ 1 . It then increases with z and levels in the intermediate sections of the disc at ~ 1 ($|\sigma_1| \gg \sigma_2$). Finally, χ_{crit} drops sharply near the surface ($\sigma_2 \gg |\sigma_1|$ again).

We now briefly turn our attention to the dependence of the magnetic coupling with height. Note that χ first increases with z , as expected, in response to the enhanced ionization fraction and lower fluid density, away from the mid-plane. Closer to the surface, it decreases again, as a result of the abrupt drop in the magnitudes of the conductivity components. In the following subsections, we explore more fully the dependence of χ versus χ_{crit} with height, which indicates which non-ideal MHD regime is locally dominant, for the disc models of interest.

4.3.1 Minimum-mass solar nebula disc

Figs 4 to 6 present curves of χ (solid lines) and $\chi_{\text{crit}} \equiv |\sigma_1|/\sigma_{\perp}$ (dashed lines) as a function of height for the fiducial model. Results are shown for $R = 1, 5$ and 10 au and different choices of the magnetic field strength. Cosmic rays are either included (top panel of each figure) or excluded from the disc (bottom panels). Bottom (solid) and leftmost (dashed) curves correspond to $B = 1$ mG in all cases. B changes by a factor of 10 between curves, except that for 5 and 10 au the top (and rightmost) curves correspond to the maximum field strength for which perturbations grow.

We note that, in all plots, the magnetic coupling near the mid-plane increases with B . In these regions of the disc, both β_i and β_e are typically $\ll 1$ (except possibly when B is very strong) and from equation (11),

$$\sigma_{\perp} \approx \frac{cen_e}{B} (\beta_i - \beta_e), \quad (67)$$

which is independent of B . As a result, $\chi \propto B^2$. On the contrary, near the surface the β_j can be very large and

$$\sigma_{\perp} \approx \frac{cen_e}{B} \frac{(\beta_i - \beta_e)}{\beta_e \beta_i} \propto \frac{1}{B^2}. \quad (68)$$

Because of this, near the surface χ is quite insensitive to changes in B , as evidenced in Figs 4 to 6.

Note that when cosmic rays are assumed to be excluded from the disc, there is a discontinuity in the curve of χ versus z/H at $R = 1$ and 5 au. This discontinuity is caused by the drop in the ionization fraction at the height where X-rays are not able to penetrate any further within the disc (see bottom panels of Figs 4 and 5). It is, therefore, not present at 10 au, because X-rays reach the mid-plane at this radius (see bottom panel of Fig. 6).

In general, when B increases, the region around the mid-plane where Hall diffusion is locally dominant ($\chi < |\sigma_1|/\sigma_{\perp}$) is reduced, as a result of the stronger magnetic coupling. At 1 au, when cosmic ray ionization is included, this criterion is satisfied in the inner sections of the disc for all magnetic field strengths of interest (Fig. 4, top panel). Above this region, there is a relatively small section where ambipolar diffusion is locally dominant while near the surface, ideal MHD holds for all magnetic field strengths.

For $R = 5$ au (Fig. 5, top panel), Hall diffusion dominates for $z/H \lesssim 2$ when $B \lesssim 10$ mG, but for $10 \text{ mG} \lesssim B \lesssim 100$ mG, ambipolar diffusion is locally dominant in the inner sections of the disc ($|\sigma_1|/\sigma_{\perp} < \chi < 10$). For stronger fields, the magnetic coupling is such that $\chi > 10$ even at the mid-plane and the fluid is in ideal-MHD

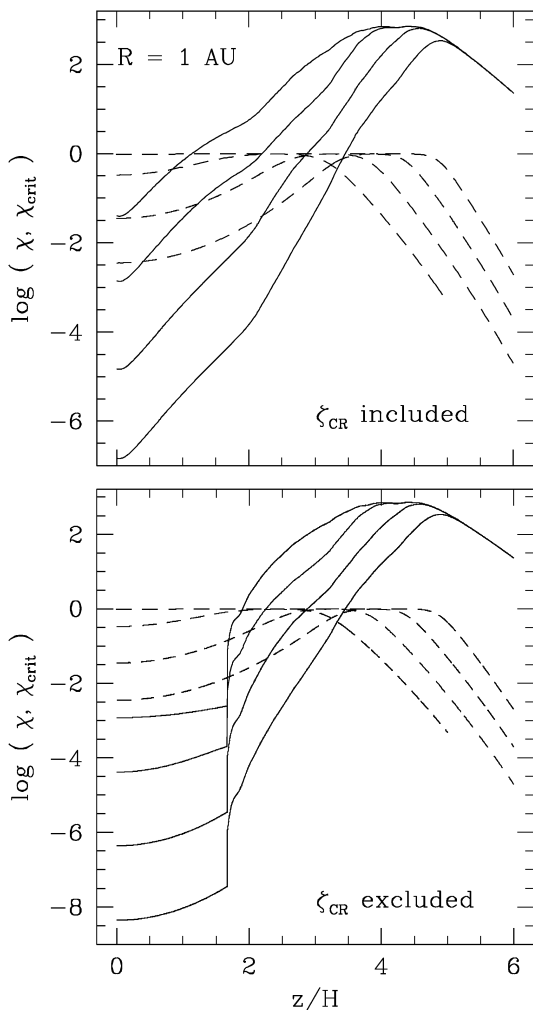


Figure 4. Comparison of the local magnetic coupling χ (solid lines) and $\chi_{\text{crit}} \equiv \sigma_1/\sigma_\perp$ (dashed lines) for the fiducial model at $R = 1$ au and different choices of the magnetic field strength. In each case, Hall diffusion is dominant in the regions where $\chi < \chi_{\text{crit}}$ (SW03). Ambipolar diffusion dominates where $\chi_{\text{crit}} < \chi \lesssim 10$. When χ is stronger than this, the fluid is in nearly ideal-MHD conditions (W99). From top to bottom (solid lines) and right to left (dashed lines), the magnetic field drops from 1 G to 1 mG. B changes by a factor of 10 between curves in all cases. Top panel: cosmic rays are present. Hall diffusion dominates for $z/H \lesssim 3.5$ to $z/H \lesssim 1$ for B increasing from 1 mG to 1 G, respectively. Bottom panel: cosmic rays are excluded from the disc by protostellar winds. Note the discontinuity in χ at the height below which X-rays are completely attenuated.

conditions over the entire cross-section of the disc. At this radius, the fluid is in the resistive regime only for very weak fields ($B \lesssim 1$ mG) and very high densities ($n_H > 10^{12} \text{ cm}^{-3}$; Wardle, in preparation). Similarly, results at $R = 10$ au (Fig. 6, top panel) show that ambipolar diffusion dominates in the inner sections of the disc for $B < 10$ mG. For stronger fields, ideal MHD is a good approximation at all z .

When cosmic rays are assumed to be excluded from the disc, the previous results at 1 au (bottom panel of Fig. 4) are largely unchanged, except for those obtained with $B = 1$ G, where Hall diffusion dominates now for $z/H \sim 1.8$, up from ~ 1 in the previous case. This is due to the sharp fall in the magnetic coupling in the region that X-rays are unable to reach. At 5 au, the Hall regime is now dominant near the mid-plane for all studied magnetic field strengths, while for $R = 10$ au there is now a Hall dominated central

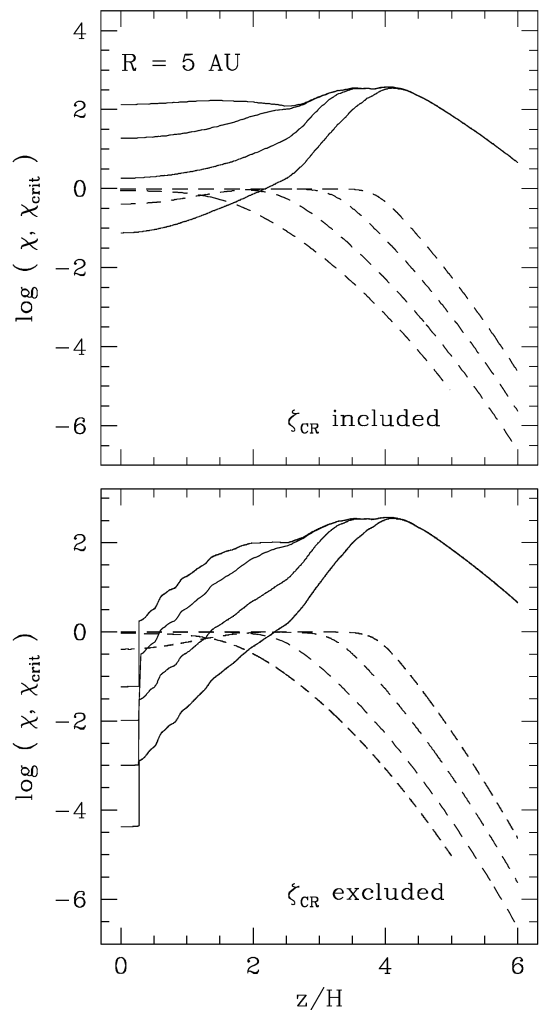


Figure 5. As per Fig. 4 for $R = 5$ au. Top (and rightmost) lines correspond here to $B = 795$ mG (top panel) and $B = 615$ mG (bottom panel), which are the maximum field strengths for which perturbations grow in each scenario. When cosmic rays are included, the Hall regime dominates near the mid-plane for $B \lesssim 10$ mG. Similarly, for $B < 100$ mG, there is an intermediate region where $\sigma_1/\sigma_\perp < \chi < 10$ and ambipolar diffusion is dominant. For stronger fields, ideal MHD holds for all z . When cosmic rays are excluded, Hall diffusion dominates near the mid-plane and ambipolar diffusion is dominant at intermediate heights, for all B of interest here.

region for $B \lesssim 10$ mG. It extends to $z/H \sim 1.3$. When $B \lesssim 100$ mG, ambipolar diffusion dominates near the mid-plane, but for stronger fields ideal MHD holds for all z .

Finally, we observe that (as expected) the magnetic coupling at the mid-plane increases with radius in response to the higher ionization fraction in the central sections of the disc at larger radii. In fact, χ_0 increases by 3–4 orders of magnitude between $R = 1$ and 10 au. On the contrary, the coupling at the surface does not change as much with radius, decreasing only from ~ 22 to ~ 2.5 between the same radii.

4.3.2 A more massive disc

Fig. 7 displays curves of χ and χ_{crit} as a function of height for a more massive disc, as detailed in Section 2.2. The ionization balance is calculated assuming that cosmic rays penetrate the disc, and results are shown for $R = 1, 5$ and 10 au for the same range of magnetic field strengths explored in the minimum-mass solar nebula model.

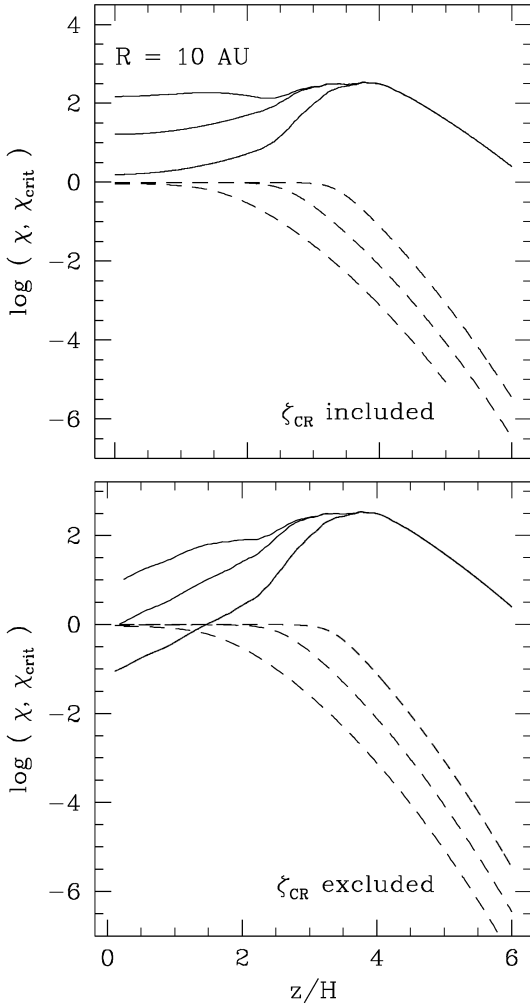


Figure 6. As per Figs 4 and 5 for $R = 10$ au. From top to bottom (and right to left), lines correspond here to $B = 100, 10$ and 1 mG. In this case, if cosmic rays are present, Hall diffusion is not dominant locally for any field strength, given the strong magnetic coupling near the mid-plane. Ambipolar diffusion dominates when $B \lesssim 10$ mG, but for stronger fields ideal MHD holds over the entire cross-section of the disc. If cosmic rays are removed, the Hall regime is relevant near the mid-plane only for $B \lesssim 10$ mG. When $B \gtrsim 100$ mG, ideal MHD holds for all z .

Increasing the surface density causes the ionization fraction near the mid-plane to drop sharply. As a result, the magnetic coupling is drastically reduced in these regions at all radii. This is especially noticeable at 1 au, where in this case X-rays are completely attenuated for $z/H < 2.6$. This, together with a very weak ionization rate ($\zeta_{\text{CR}} \sim 10^{-18}$ for $z/H \approx 2.6$ and it is negligible at $z = 0$), causes χ to be very low (and only weakly dependent on z) in this section of the disc.

The weaker coupling at low z results in Hall diffusion being locally dominant over a larger cross-section of the disc in this model. We find that, for $R = 1$ au, there is again a Hall dominated region about the mid-plane for all studied B . This section now extends to $z/H \sim 2.3$ for $B = 1$ G, up from $z/H \sim 1$ in the minimum-mass solar nebula disc. For weaker fields, these regions are also larger.

For $R = 5$ au, Hall diffusion is now dominant near the mid-plane for $B < 1$ G. For comparison, in the previous case Hall conductivity was locally important for $B < 10$ mG. Furthermore, ambipolar

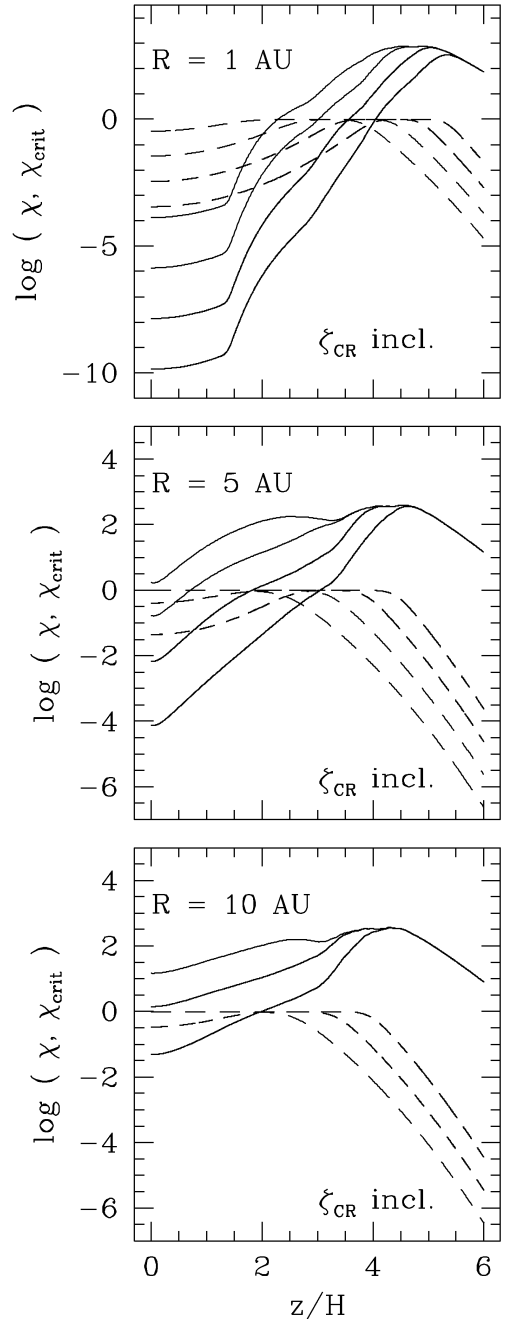


Figure 7. As per Figs 4 to 6 for $R = 1, 5$ and 10 au for a more massive disc, such that $\Sigma'_0 = 10\Sigma_0$ and $\rho'_0 = 10\rho_0$. Cosmic rays are present. From top to bottom (and right to left), lines correspond to $B = 1, 0.1, 10^{-2}$ and 10^{-3} G ($R = 1$ and 5 au), and $B = 0.1, 10^{-2}$ and 10^{-3} G ($R = 10$ au). The increased surface density causes the magnetic coupling to drop near the mid-plane. As a result, Hall conductivity dominates over a larger section of the disc around the mid-plane, while ambipolar diffusion is important (at higher z) for stronger fields than it was the case in the minimum-mass solar nebula model.

diffusion dominates over a small cross-section of the disc for all but the strongest ($B \gtrsim 1$ G) magnetic field strengths at this radius. This contrasts with the previous case, where ideal MHD held at all z when $B \gtrsim 100$ mG. Even at 10 au, Hall diffusion now dominates near the mid-plane when $B \lesssim 10$ mG. When B is stronger than this, but still $\lesssim 100$ mG, ambipolar diffusion predominates for $z/H \lesssim 2$,

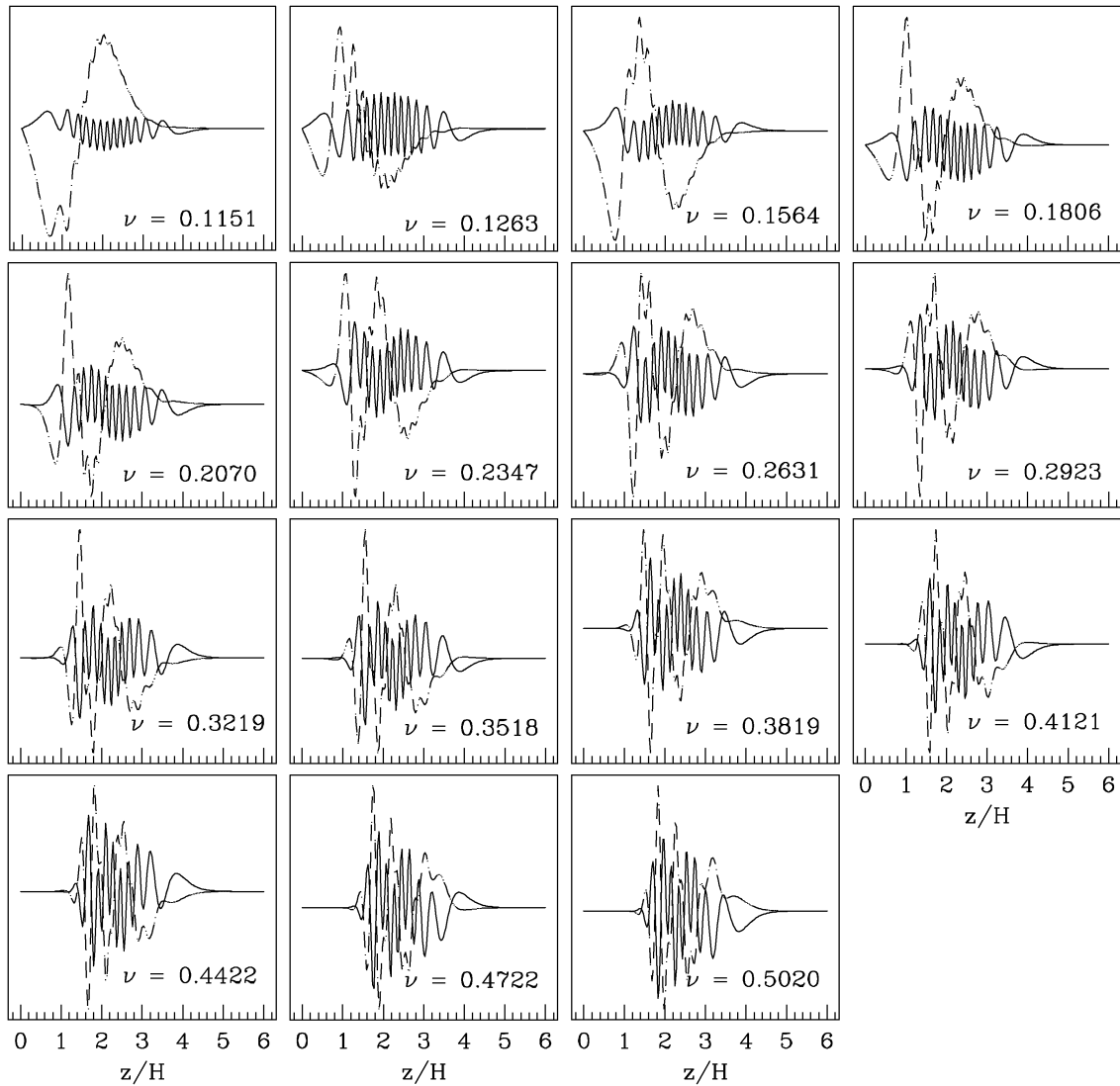


Figure 8. Structure of all unstable modes for the fiducial model at $R = 1$ au and $B = 100$ mG. In each case, solid lines show δB_r , while dashed ones correspond to δB_ϕ . The growth rate is indicated in the lower right corner of each panel. There are 15 unstable modes, with $0.1151 \leq \nu \leq 0.5020$. Some perturbations grow at the mid-plane, particularly when $\nu < 0.1806$. Modes growing faster than this show a dead region around the mid-plane, whose vertical extent increases with the growth rate of the perturbations. Note the asymmetry of δB_r and δB_ϕ about zero, especially in slowly growing modes.

while in the minimum-mass solar nebula, ideal MHD held for $B \gtrsim 10$ mG.

In the next section, we analyse the effect of different conductivity regimes being dominant at different heights, in the structure and growth rate of MRI perturbations. Different disc models, radial locations and magnetic field strengths are discussed.

5 MAGNETOROTATIONAL INSTABILITY

5.1 Structure of the perturbations

5.1.1 All unstable modes at 1 au

Fig. 8 shows the structure and growth rates of all unstable MRI perturbations for the fiducial model at 1 au and $B = 100$ mG. Solid lines denote δB_r , while dashed lines correspond to δB_ϕ . This notation is observed in this paper in all plots that display the structure of the instability.

The fastest growing perturbation in this case grows at $\nu = 0.5020$ and there are 15 unstable modes with $0.1151 \leq \nu \leq 0.5020$. Slow growing perturbations, with $\nu < 0.1806$, are active even at the mid-plane, while faster modes exhibit a central magnetically inactive (dead) zone (Gammie 1996; Wardle 1997). Moreover, the extent of the dead zone increases with the growth rate and for the fastest growing mode it extends to $z/H \sim 1.6$. We observe that δB_r and δB_ϕ , especially in the slow growing modes, are asymmetrical about zero and their averages over vertical sections of the disc have opposite signs. This appears to be related to the dependence of these two fluid variables in equation (47).

5.1.2 Most unstable modes at different radii, including cosmic ray ionization

The weakest strength for which unstable modes could be computed was 1 mG. This is a computational, rather than a physical limit: the dependence of ν_{\max} with B in the weak-field limit shows no

evidence for a minimum required field strength for the instability to grow (see Section 5.2.1). A comparison of the structure of the most unstable modes for the fiducial model at $R = 1, 5$ and 10 au is shown in Fig. 9. We display solutions for B from 1 mG, up to the maximum field strength for which unstable modes grow for each radius. Unless stated otherwise, this criterion is followed in all plots that show the structure of the fastest growing modes as a function of B in this study. Note that the maximum value of B is dependent on the disc model, the ionizing agents incorporated and radius of interest.

Both the structure and growth rate of these perturbations are shaped by the competing action of different conductivity components, whose relative importance changes with height. We defer the analysis of their growth rate to Section 5.2. Here, we discuss the structure as a function of z . Note first of all that, at each radius, the wavelength of the perturbations increases with the magnetic field strength, as expected by both ideal MHD and non-ideal MHD local analyses (Balbus & Hawley 1991; W99).

At 1 au (leftmost column of Fig. 9), for $B \lesssim 500$ mG, the region next to the mid-plane is a magnetically inactive zone (Gammie 1996; Wardle 1997). The extent of this region decreases as the field gets stronger. For example, for $B = 1$ mG it extends from the mid-plane to $z/H \sim 1.8$, but when $B > 500$ mG, there is no appreciable dead region, a result of the stronger magnetic coupling close to the mid-plane and the relatively small wavenumber of the perturbations. Also, at this radius, when B is relatively strong ($B > 500$ mG), the amplitude of these modes increases with z , a property that is typical of MRI perturbations driven by ambipolar diffusion. Ambipolar diffusion modes have this property because, as the local analysis (W99) indicates, in this limit the local growth of unstable modes increases with the magnetic coupling, which (except in the surface regions) increases with z (see Fig. 3). As a result, the local growth rate of the MRI also increases with height in this regime and is able to drive the amplitude of global unstable modes to increase. This explains the shape of the envelope of these modes. Finally, note that, when the magnetic field is weak, the wavenumber of the perturbations is very high, and δB_r and δB_ϕ are not symmetrical about $z = 0$.

At 5 au, when $B \gtrsim 100$ mG, perturbations grow even at the mid-plane. For weaker fields, they exhibit only a very small dead zone, which extends to $z/H \lesssim 0.5$. Note also that the envelope of these modes, particularly for $B \gtrsim 100$ mG, is fairly flat. This is explained by recalling that the magnetic coupling at the mid-plane in this region is very high ($\chi \sim 90$ for $B = 500$ mG, Fig. 5, top panel), so the ideal-MHD approximation holds. Under these conditions, unstable modes peak at the node closest to the mid-plane, given that the local growth rate is not a strong function of χ and does not vary by much with height (see also top row of Fig. 6 of SW03, which shows similar envelopes for perturbations obtained with $\chi_0 = 100$ and different configurations of the conductivity tensor). On the other hand, for $B \lesssim 100$ mG, non-ideal MHD effects are important. When $B = 10$ mG, ambipolar diffusion is dominant for $z/H \lesssim 2.3$. This conductivity term is likely to drive the structure of this perturbation, as evidenced by the central dead zone and the envelope peaking at an intermediate height. For $B = 1$ mG, Hall conductivity is dominant close to the mid-plane ($z/H \lesssim 2$), the region where the envelope of this perturbation peaks. Furthermore, the high wavenumber suggests that its structure is determined by local effects. As a result, Hall conductivity is likely to drive the structure of this mode.

Finally, for $R = 10$ au there is no appreciable dead zone for $B \gtrsim 10$ mG, given the strong magnetic coupling at this radius. Even for $B = 1$ mG, $\chi_0 \sim 3$, a figure that increases to ~ 100 for

$B = 100$ mG. As a result, the fluid is in nearly ideal-MHD conditions (see Section 4.3.1), which explains the flat envelope of these modes.

5.1.3 Most unstable modes at different radii, excluding cosmic ray ionization

We also calculated the structure of the most unstable modes at the same three radial positions under the assumption that cosmic rays are excluded from the disc by protostellar winds (Fig. 10). In this case, the central dead zones at 1 au ($B \lesssim 100$ mG) extend over a larger cross-section of the disc, given that cosmic rays (when present) are the main source of ionization near the mid-plane at this radius (see Section 4.2). Without them, the electron fraction below $z/H \sim 1.7$ (where X-rays are completely attenuated) plummets, causing the amplitude of MRI perturbations in this section of the disc to be severely reduced. As a result, when $B \lesssim 100$ mG, perturbations are damped for $z/H \lesssim 2$. Another difference with the previous case is noticeable for stronger fields ($B \gtrsim 500$ mG), where before the MRI was active even at the mid-plane. In this case, the abrupt change in the ionization balance at the height where X-ray ionization becomes active (Fig. 1, top panel) causes the current to be effectively discontinuous there and produces the observed kink in the amplitude of these modes.

In the zone where X-rays are excluded ($z/H \lesssim 1.7$), the main ionizing agent is the decay of radioactive elements within the disc. However, they can only produce very weak magnetic coupling. For example, $\chi_0 \sim 10^{-8}$ for $B = 1$ mG and it only increases to $\sim 10^{-3}$ when $B = 1$ G. As a result, the amplitude of the perturbations near the mid-plane, even for strong fields ($B \gtrsim 500$ mG), is very small at this radius. If the abundance of metals in the gas phase is reduced from the fiducial value adopted here ($\delta_2 \approx 0.02$) to (say) $\sim 2 \times 10^{-3}$, the zone ionized only by radioactivity becomes magnetically dead (as expected). The growth of the perturbations is only marginally affected.

For $R = 5$ au, we also observe a small kink in the amplitude of the perturbations for $B \gtrsim 100$ mG. In this case, it occurs much closer to the mid-plane, because at this radius X-rays penetrate to $z/H \sim 0.3$. Finally, for $R = 10$ au, X-rays penetrate the entire cross-section of the disc, so there is no kink in the amplitude of these modes. However, the mid-plane cosmic ray ionization rate at this radius is about 2 orders of magnitude larger than that of X-rays (in fact they dominate over X-rays for $z/H \lesssim 2.5$, see Fig. 1, bottom panel), so excluding them does reduce significantly the magnetic coupling in this region. As an illustration of this, note that, for $B = 10$ mG, χ_0 decreases from ~ 16 in the previous case to only ~ 1 here (see Fig. 6). As a result, for $z/H \lesssim 0.3$ the fluid is in the Hall regime while ambipolar diffusion dominates at higher z . Being a high-wavenumber perturbation, the structure of this mode reflects mainly local fluid conditions. This explains the shape of its envelope (see rightmost column of Fig. 10, second panel from the top): a flat envelope close to the mid-plane where the Hall effect is dominant and amplitude increasing with z at higher vertical locations, driven by ambipolar diffusion. Finally, for $B = 1$ mG, $\chi < |\sigma_1|/|\sigma_\perp|$ for $z/H < 1.3$. This, together with the high wavenumber of the perturbations, causes Hall diffusion to shape the envelope of this mode.

5.1.4 Conductivity regime comparison ($\sigma_1 B_z > 0$)

It is interesting to compare the structure of the most unstable perturbations obtained with different configurations of the conductivity

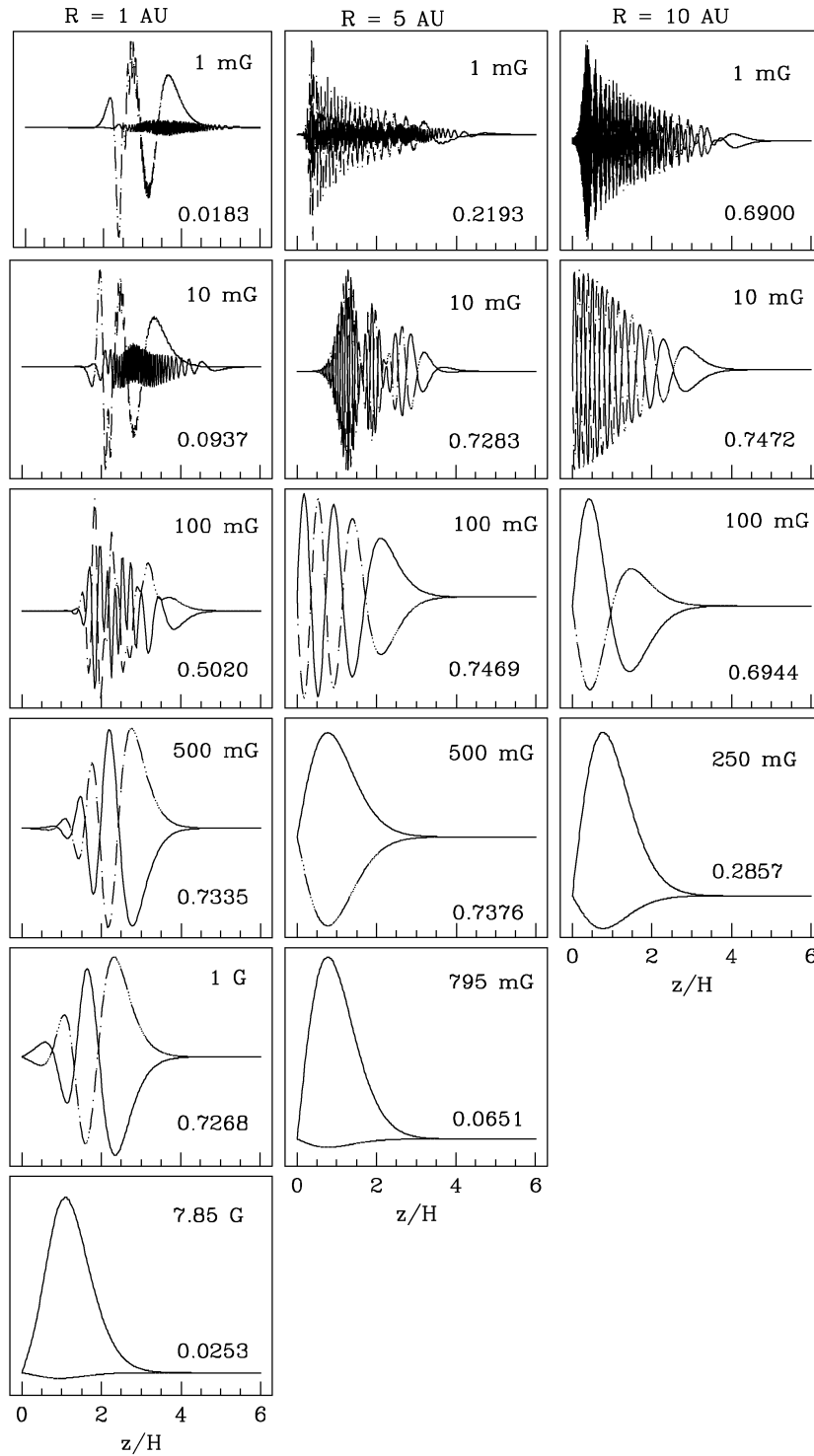


Figure 9. Comparison of the structure of the most unstable modes for the fiducial model at $R = 1, 5$ and 10 au for different choices of the magnetic field strength. B is indicated in the upper right-hand of each panel while the growth rate is shown in the bottom right-hand side. Results are shown for B spanning from 1 mG, the weakest magnetic field strength for which unstable modes could be computed, to the maximum strength for which unstable modes grow, which changes with the radius. Note that for all three radii, the wavelength of the perturbations increases with the strength of the magnetic field, as expected. At 1 au, for $B < 500$ mG, there is a central dead zone, which extends to $z/H \lesssim 2$. At 5 au, only modes for $B < 100$ mG exhibit a dead region. For stronger fields, the magnetic coupling, even at the mid-plane, is sufficiently large for ideal MHD to be a good approximation. Finally, for $R = 10$ au, ideal MHD holds throughout the cross-section of the disc for $B \gtrsim 10$ mG and perturbations in this region of parameter space grow even at the mid-plane.

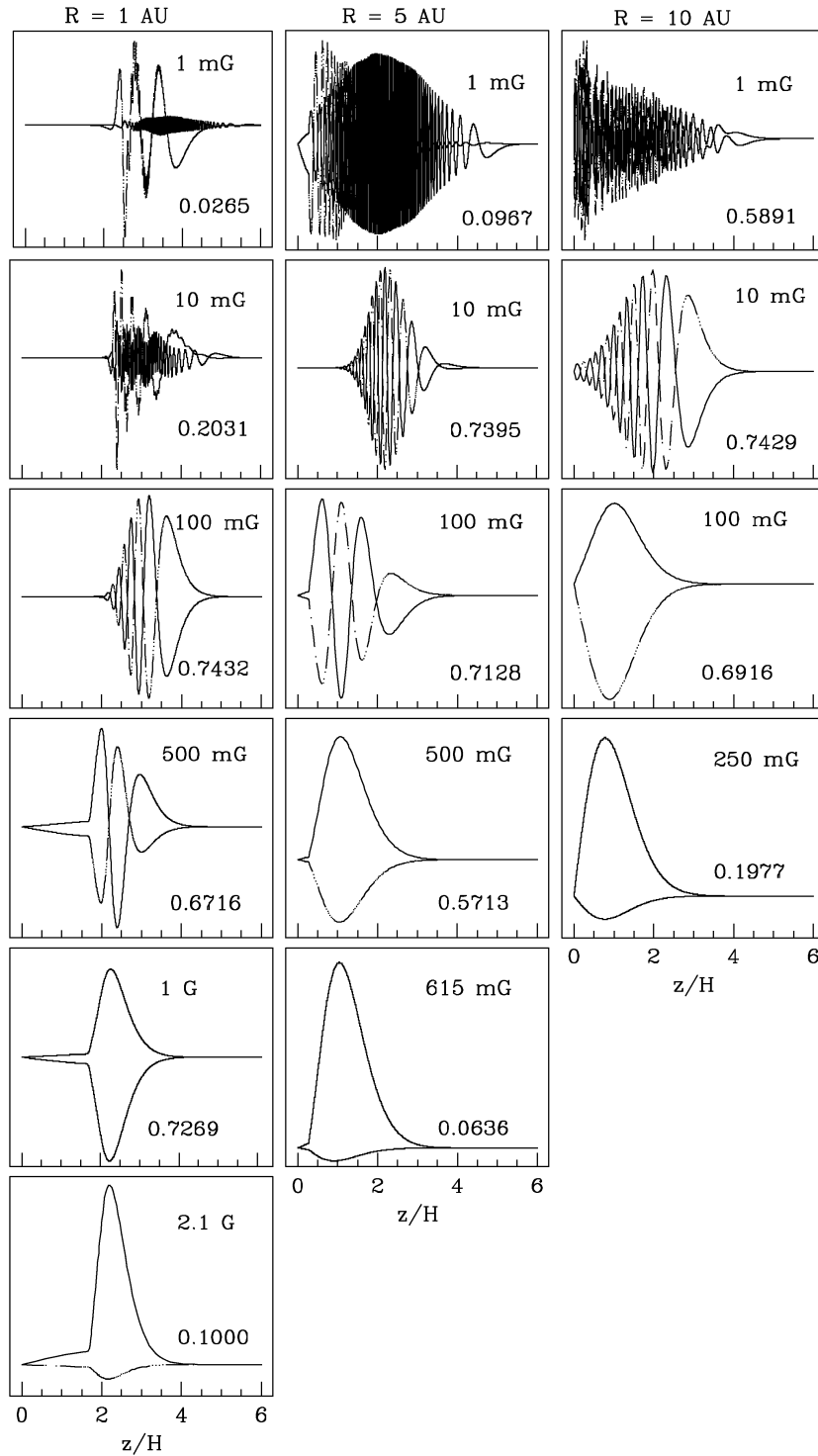


Figure 10. As per Fig. 9 assuming cosmic rays are excluded from the disc. Note the increased extent of the central dead zone at 1 au ($B \lesssim 100$ mG) and the kink in the amplitude of the perturbations for stronger fields. This feature is caused by the sharp change in the ionization balance of the disc at the height where X-ray ionization becomes active. As expected, this effect is less pronounced at 5 au and unnoticed at 10 au, where X-rays reach the mid-plane.

tensor (assuming that different conductivity regimes dominate over the entire cross-section of the disc) against the full conductivity results discussed in Section 5.1.2. This way we can explore more fully the effects of different conductivity components in the overall properties of the instability. Fig. 11 presents such solutions for the fiducial model at $R = 1$ au as a function of the strength of the magnetic field. The left column shows solutions computed with a full

conductivity tensor, while the middle and right ones display modes obtained using the ambipolar diffusion ($\sigma_1 = 0$) and Hall regime ($\sigma_2 = 0, \sigma_1 B_z > 0$) approximations, respectively.

Note that, for all magnetic field strengths shown here, perturbations computed using the ambipolar diffusion approximation have a more extended central dead zone than modes incorporating a full conductivity tensor. This is in agreement with the local analysis

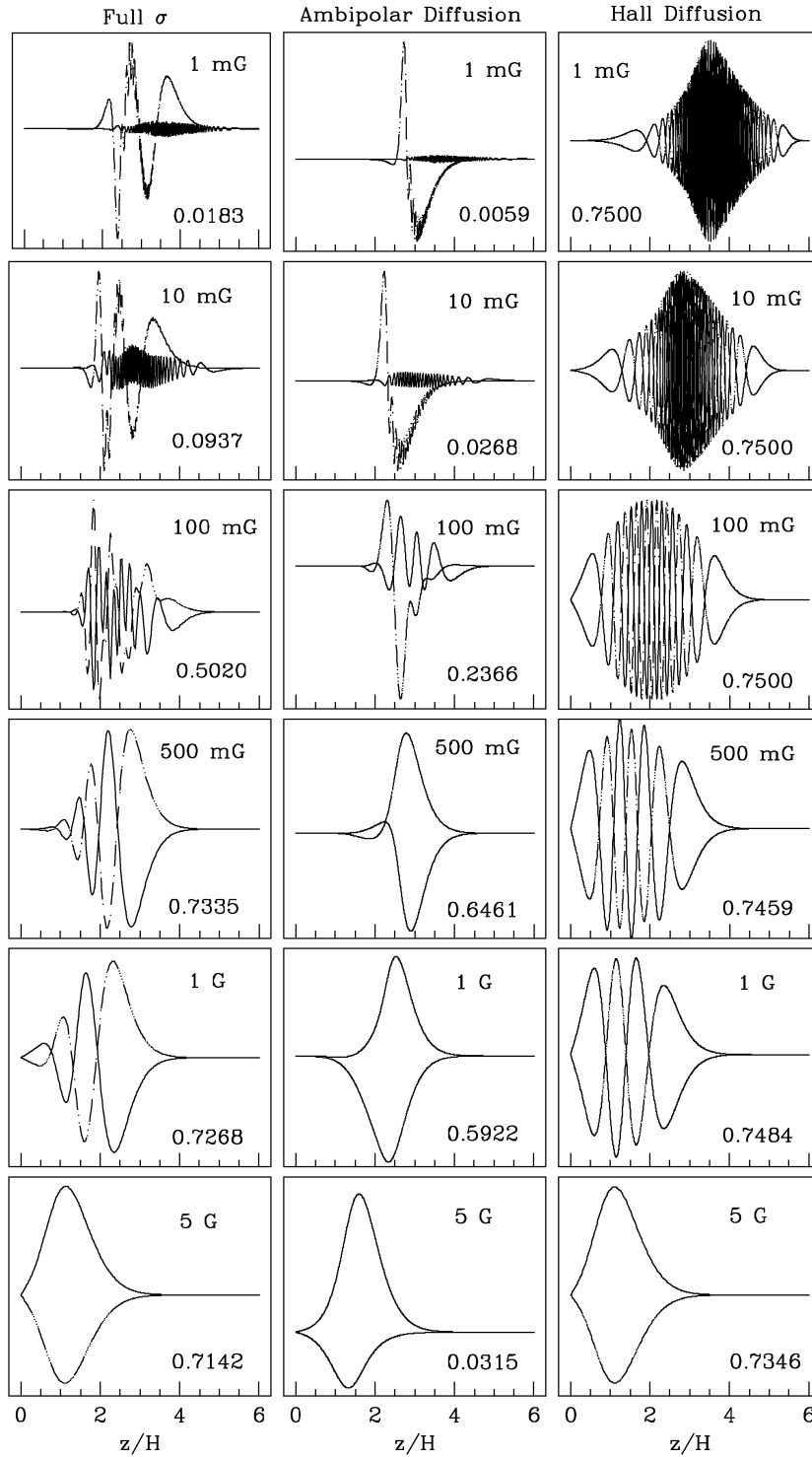


Figure 11. Comparison of the structure of the most unstable modes of the MRI for the fiducial model at $R = 1$ au as a function of the magnetic field strength for different configurations of the conductivity tensor. The field strength spans from 1 mG up to 5 G, which is the maximum B for which perturbations grow in the ambipolar diffusion regime. The left column shows solutions obtained with a full conductivity tensor. The middle and right columns correspond to the ambipolar diffusion ($\sigma_1 = 0$) and Hall ($\sigma_2 = 0, \sigma_1 B_z > 0$) approximations, respectively. Note that, when the magnetic field is weak ($B \lesssim 100$ mG), full conductivity perturbations have a higher wavenumber and grow closer to the mid-plane, than modes in the ambipolar diffusion limit. This reflects the contribution of the Hall effect. For stronger fields, the shape of the envelope appears to be driven by ambipolar diffusion (amplitude increases with height), with the Hall term increasing the wavenumber of the perturbations.

(W99), which showed that the growth of MRI perturbations in the ambipolar diffusion limit decreases steadily with the local magnetic coupling. As a result, the local growth of these modes is severely restricted near the mid-plane. This is especially effective for weaker fields, when global effects are less important due to the high wavenumber of the perturbations. For example, when $B = 1$ mG, the magnetically dead zone in modes found using the ambipolar diffusion approximation extends to $z/H \sim 2$. The thickness of the dead region decreases for stronger B , but even with $B = 1$ G, there is a small section ($z/H \lesssim 0.5$) in which perturbations do not grow.

Turning now our attention to Hall perturbations, we observe that their amplitude is fairly stable, especially for strong fields ($B \gtrsim 500$ mG), where they show the characteristic flat envelope reported by SW03. When the field is weaker than this, perturbations are damped near the mid-plane. This is particularly evident for $B < 100$ mG and is probably related to the fact that at 1 au the magnetic coupling at the mid-plane in this limit is very low. Even for $B = 100$ mG, χ_0 in the Hall limit is $\sim 10^{-4}$ and it decreases to $\sim 10^{-10}$ for $B = 1$ mG (note that these values are significantly smaller than the ones shown in Fig. 4, which were obtained with a full conductivity tensor). Local results highlight that the maximum local growth rate of MRI perturbations in the Hall limit is effectively unchanged from the ideal case when $\chi \rightarrow 0$ (W99). However, the global analysis presented here shows that, when the coupling is very low, the amplitude of global Hall limit perturbations can be damped close to the mid-plane (see rightmost column of Fig. 11, top three panels). On the other hand, there is only a small dead zone for $B \sim 1$ mG, which extends from the mid-plane to $z/H \sim 0.5$. For stronger fields, there is no appreciable dead region.

In general, the structure of full σ perturbations reflects the contribution of Hall as well as ambipolar diffusion conductivity terms. When the magnetic field is strong ($B > 100$ mG), ambipolar diffusion is locally dominant over a more extended section of the disc and the dead zone of perturbations in this limit is smaller than it is for weaker fields. On the other hand, modes in the Hall limit grow now even at the mid-plane and have a significantly higher wavenumber than ambipolar diffusion perturbations. This is reflected in the structure of full σ modes in this region of parameter space: their envelope is shaped by ambipolar diffusion (the amplitude increases with height), but the wavenumber is higher and they grow closer to the mid-plane than pure ambipolar diffusion modes do. This reflects the contribution of the Hall effect. These results are also in agreement with similar trends found with illustrative calculations in SW03.

It was discussed in Section 4.3 that, at this radius (1 au), Hall conductivity is locally dominant near the mid-plane for all magnetic field strengths of interest. The transition to the zone where ambipolar diffusion dominates occurs at a lower z for stronger fields (Fig. 4, top panel). This analysis reveals that the Hall effect modifies the structure of MRI modes even when Hall diffusion is locally dominant only for a small section close to the mid-plane of the disc. In Section 5.2.1, it will be discussed how the Hall effect also alters the growth of all the fastest growing modes at this radius.

At 5 au, ambipolar diffusion is important in the inner sections of the disc for $B \lesssim 100$ mG (Fig. 5). It is expected that perturbations obtained using this approximation will be different from the corresponding full σ modes in this region of parameter space. Fig. 12 compares solutions obtained with different configurations of the conductivity tensor at this radius. Ambipolar diffusion modes (left column) are indeed different from full σ ($\sigma_1 B_z > 0$) ones (middle column) when $B \lesssim 100$ mG. For stronger fields,

ideal MHD holds, so the structure of MRI modes computed using different configurations of the conductivity tensor are alike, as expected.

5.1.5 Conductivity regime comparison ($\sigma_1 B_z < 0$)

So far we have discussed solutions obtained with a $\sigma_1 B_z > 0$ Hall conductivity term, which corresponds to the case where the magnetic field and angular velocity vectors of the disc are parallel ($\Omega \cdot B > 0$). We now explore how these results are modified when these vectors are antiparallel.

As noted before, we explored in this case a reduced region of parameter space. In particular, solutions at 1 au could not be computed at all, as $\chi_0 \ll 2$ for all B of interest at this radius, the limit below which all wavenumbers grow in this regime (W99; see also Section 4.1). On the other hand, results at 10 au do not differ appreciably in this case from those obtained using a $\sigma_1 B_z > 0$ conductivity, given the strong magnetic coupling throughout the cross-section of the disc at this radial location. At 5 au, however, Hall diffusion is important for relatively weak fields ($B \lesssim 10$ mG) and both sets of results should be different in this region of parameter space. Fig. 12 (middle and right columns) compares the structure of MRI unstable modes computed with a positive and negative Hall conductivity at this radius, as a function of the magnetic field strength. When $\sigma_1 B_z < 0$, no results could be computed for $B < 8$ mG, as $\chi_0 < 2$ in these cases. We find that, indeed, for $B = 10$ mG the most unstable mode computed with a negative Hall conductivity has a higher wavenumber and a slower growth rate, than the corresponding mode with $\sigma_1 B_z > 0$.

5.1.6 More massive disc

To finalize the analysis of the structure of MRI perturbations, we describe now the properties of unstable modes in a more massive disc, as characterized in Section 2.2. Results are displayed in Fig. 13. As expected, the larger column density causes unstable modes to have a more extended central dead zone in relation to results in the minimum-mass solar nebula model. This is particularly noticeable for $R = 1$ au, where there is now a magnetically inactive zone for $B \lesssim 1$ G. X-rays are excluded from the mid-plane at this radius (they can only penetrate up to $z/H \sim 2.6$ for this disc model) and the cosmic ray ionization rate at $z = 0$ is negligible. As a result, even for $B = 1$ G the magnetic coupling at the mid-plane is $\sim 10^{-4}$, which causes perturbations to be damped at low z . We observe here the same trends discussed in the analysis of the minimum-mass solar nebula model in relation to the structure of these modes. Ambipolar diffusion shapes the envelopes, particularly for strong fields, while Hall diffusion increases their wavenumber in comparison with results in the ambipolar diffusion limit. Finally, note the kink on the amplitude of the $B = 5.85$ G mode, attributed to the sharp increase in the ionization fraction at the height where X-ray ionization becomes active.

At 5 au, there is also a more extended dead zone, observed up to $B \sim 100$ mG, in comparison with that of perturbations obtained using the minimum-mass solar nebula model. In that case, ideal-MHD conditions held throughout the cross-section of the disc for $B = 100$ mG, with $\chi_0 \sim 20$ (see Section 5.1.2). On the contrary, in the present model, $\chi_0 \sim 0.2$ for this magnetic field strength and ambipolar diffusion is locally dominant for $0.7 \lesssim z/H \lesssim 2$ (see Fig. 7, middle panel). As a result, the amplitude of this perturbation increases with z , a typical behaviour of ambipolar diffusion driven MRI, instead of being flat as before.

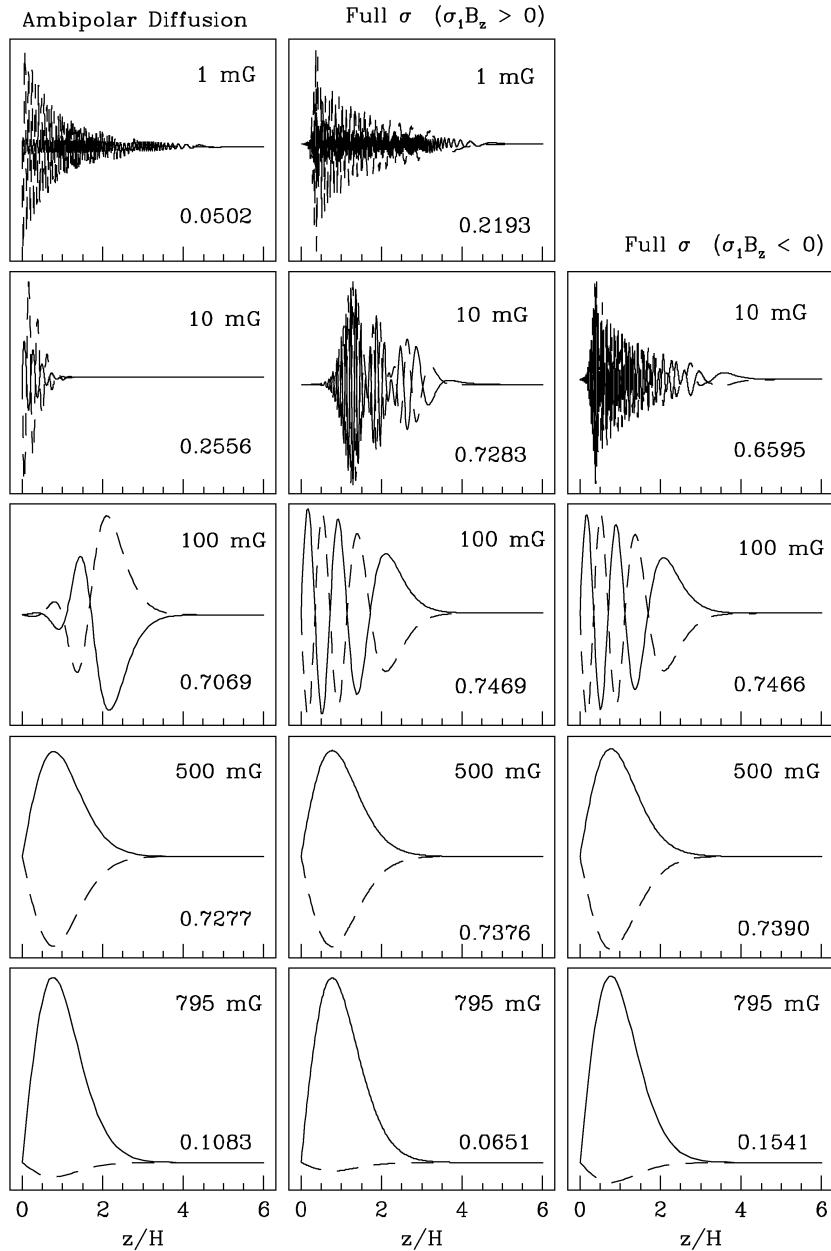


Figure 12. Comparison of the structure of the fastest growing modes for the fiducial model at $R = 5$ au, for different configurations of the conductivity tensor. The left column corresponds to the ambipolar diffusion approximation. The middle and right columns show solutions obtained with a full conductivity tensor when the magnetic field and angular velocity vectors of the disc are parallel ($\sigma_1 B_z > 0$) and antiparallel ($\sigma_1 B_z < 0$), respectively. Note that when $B \lesssim 10$ mG, full σ solutions obtained with Hall conductivity terms of opposite signs are different, as this component dominates near the mid-plane in this region of parameter space. On the other hand, ambipolar diffusion perturbations differ from full σ ones for $B \lesssim 100$ mG, given that, for these magnetic field strengths, σ_2 dominates close to the mid-plane. For stronger fields, the fluid is in nearly ideal-MHD conditions and perturbations in all three configurations of the conductivity tensor are alike.

Finally, for $R = 10$ au, ideal-MHD conditions hold throughout the disc cross-section for $B \gtrsim 100$ mG (Fig. 7, bottom panel). Because of this, the envelopes are flat in this region of parameter space (see Fig. 13, right column, lower two panels). On the other hand, when $B \sim 10$ mG, $\chi_0 \sim 1.5$ and ambipolar diffusion dominates up to $z/H \sim 2$. As a result, this mode exhibits a small central dead zone and the envelope peaks at an intermediate height. Finally, when $B \sim 1$ mG, $\chi_0 \sim 0.05$ and Hall diffusion is dominant for $z/H \lesssim 2$. Consequently, the central dead zone is much reduced and this per-

turbation grows closer to the mid-plane despite the weak magnetic coupling.

5.2 Growth rate of the perturbations

5.2.1 Fastest growing modes for different conductivity regimes

The dependence of the growth rate of the most unstable modes with the strength of the magnetic field is shown in Fig. 14 for different

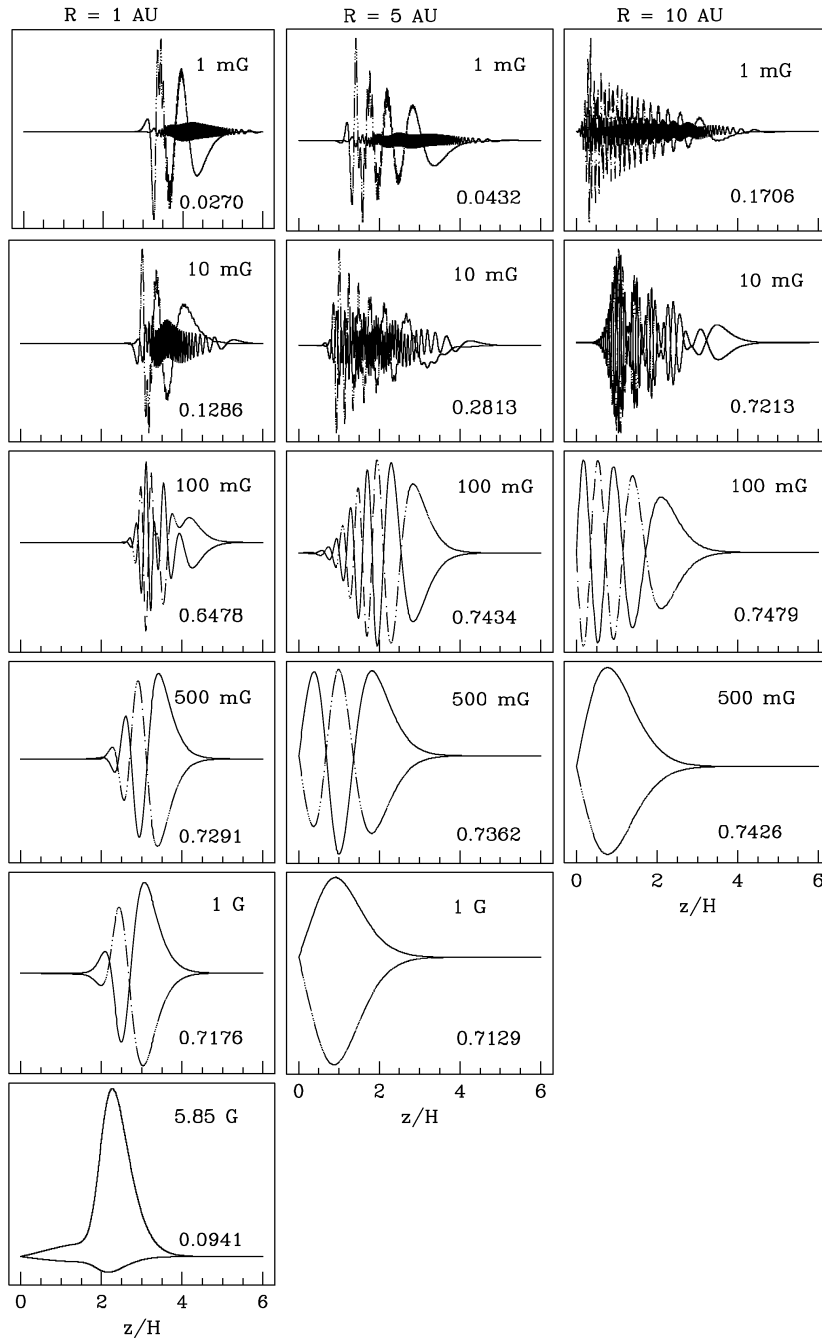


Figure 13. Comparison of the structure of the most unstable modes of the MRI for a more massive disc, incorporating cosmic ray ionization. We present results at $R = 1, 5$ and 10 au as a function of the strength of the magnetic field. The disc surface and mass density are $\Sigma'_0 = 10 \Sigma_0$ and $\rho'_0 = 10 \rho_0$. For simplicity, it was assumed that the temperature, sound speed and scaleheight are unchanged from those of the minimum-mass solar nebula model. Note that these modes have a more extended central dead zone, especially for $R = 1$ au, in relation to the fiducial model. The kink in the perturbation at $R = 1$ au for $B = 5.85$ G (leftmost column, bottom panel) is caused by the sudden change in the ionization balance at the height where X-rays are not able to penetrate further within the disc.

configurations of the conductivity tensor. Results correspond to the fiducial model at $R = 1$ au (top panel) and 10 au (bottom panel). We will use Fig. 12 to analyse the corresponding results at 5 au.

The overall dependence of the ν_{\max} versus B curve for full σ modes is typically as follows: ν_{\max} initially increases with B with an approximate power-law dependence. It then levels at ~ 0.75 , the maximum growth rate for ideal-MHD perturbations in Keplerian discs. Eventually, the maximum growth rate decays sharply at a

characteristic magnetic field strength at which the wavelength of the perturbations is $\sim H$, the scaleheight of the disc. Note that in the weak-field limit, the dependence of the ν_{\max} versus B curve shows no evidence of a minimum field strength, below which modes do not grow. This characteristic shape of the ν_{\max} versus B curve can be explained in terms of the dependence of the growth rate of the perturbations on B when different conductivity components are dominant at different heights.

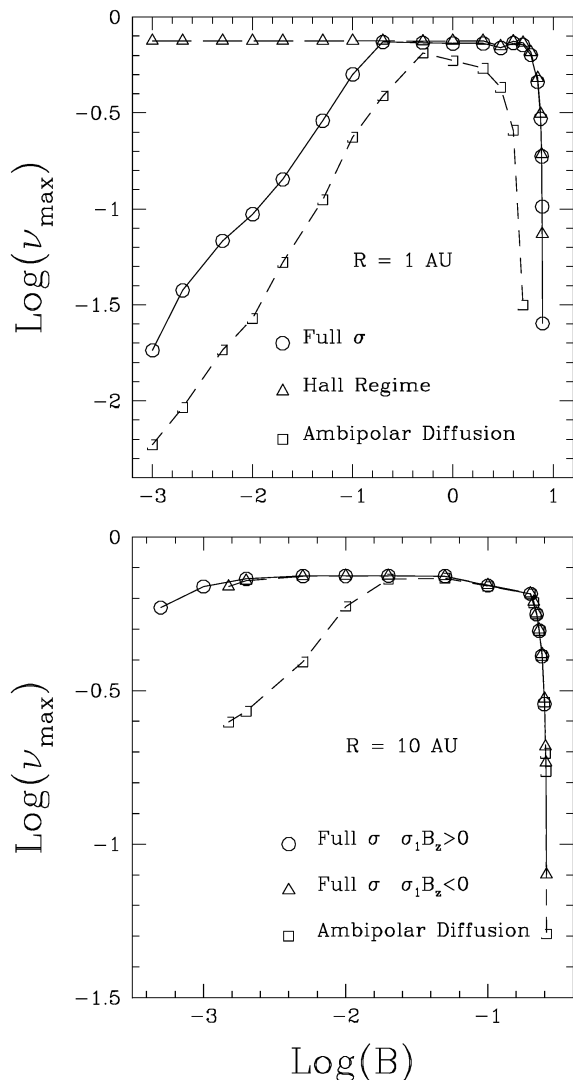


Figure 14. Growth rates of the fastest growing modes as a function of the strength of the magnetic field for different configurations of the conductivity tensor. Results are presented at $R = 1$ au (top panel) and 10 au (bottom panel) for the fiducial model. It is evident that, at 1 au, when the magnetic field is weak ($B \lesssim 200$ mG), perturbations are driven by ambipolar diffusion. As a result, ν_{\max} increases with B . As the field gets even stronger, the maximum growth rate of full σ and Hall limit perturbations are practically identical, signalling that Hall conductivity determines the growth of global unstable modes in this region of parameter space. Finally, ν_{\max} decreases rapidly when B is so strong that the wavelength of the fastest growing mode is approximately the scaleheight of the disc.

Examining Fig. 14 (top panel), it is clear that, for weak fields ($B \lesssim 200$ mG), perturbations computed with a full σ have a ν_{\max} versus B dependence similar to that of solutions obtained using the ambipolar diffusion approximation. This indicates that this feature is driven by ambipolar diffusion. In this limit, the local maximum growth rate of MRI modes increases with the magnetic coupling (W99), which in turn, increases with B , except when β_i and $|\beta_e| \gg 1$ (e.g. near the surface). As a result, ν_{\max} should increase with B , as observed. On the contrary, when the magnetic field is stronger than ~ 200 mG, the growth rate of MRI modes obtained with a full conductivity tensor is practically identical to that of Hall limit modes. In this region of parameter space, the growth rate of global

modes remains unchanged when the magnetic field gets stronger, as expected when Hall diffusion drives the growth of the instability. Eventually, B becomes strong enough that the wavelength of the fastest growing mode becomes of the order of the scaleheight of the disc and the growth rate rapidly declines. These results are in agreement with previous findings by W99 and SW03.

Note also that the maximum growth rate of perturbations in the Hall limit does not change appreciably with B , until they are damped for a sufficiently strong field, as expected. In fact, Hall perturbations grow at approximately the ideal-MHD rate even for $B \sim 1$ mG.

Hall diffusion is locally dominant at 1 au in the lower sections of the disc for all magnetic field strengths for which unstable modes exist (Fig. 4, top panel). As a result, perturbations obtained with a full conductivity tensor grow significantly faster than modes found using the ambipolar diffusion approximation for all B .

For $R = 5$ au, the Hall effect increases the growth rate of full σ perturbations when $B \lesssim 10$ mG, the region of parameter space where Hall diffusion is locally dominant near the mid-plane (compare the growth rates in left and middle columns of Fig. 12). Moreover, full σ modes computed with $\sigma_1 B_z > 0$ (middle column) and $\sigma_1 B_z < 0$ (right column) grow at different speeds and have different structure, as expected in the region where Hall diffusion dominates.

Finally, Fig. 14 (bottom panel) displays the growth rate of the most unstable modes at 10 au. Results were computed with a full conductivity tensor (but with opposite signs of $\Omega \cdot B$), as well as using the ambipolar diffusion approximation. In this case, Hall diffusion is locally unimportant for all B studied here, so the sign of $\sigma_1 B_z$ does not affect the growth of the perturbations. On the other hand, at this radius, ambipolar diffusion is important for $B \lesssim 10$ mG. This slows the growth of perturbations in the ambipolar diffusion limit when the magnetic field is weaker than this value.

5.2.2 Fastest growing modes at different radii

We also compare the growth rate of the most unstable modes at different radii as a function of the strength of the magnetic field (Fig. 15). Three sets of results are displayed. The first two correspond to the minimum-mass solar nebula disc assuming cosmic rays either penetrate the disc (top panel) or are excluded from it (middle panel). The last set presents results for the more massive disc model (bottom panel), incorporating cosmic ray ionization. Note that in all three cases, MRI perturbations grow over a wide range of magnetic field strengths.

The maximum field strength for which unstable modes exist (within each panel), is weaker at larger radii. In ideal-MHD conditions, as well as when either the ambipolar diffusion or Hall ($\sigma_1 B_z > 0$) conductivity regimes dominate, unstable MRI modes are damped when $v_A/c_s \sim 1$ (Balbus & Hawley 1991), which corresponds to $\lambda \sim H$. In the Hall ($\sigma_1 B_z < 0$) limit, unstable modes have been found for $v_A/c_s \sim 3$ (SW03, albeit using a constant conductivity profile). In any case, as both the gas density (equation 26) and the sound speed (equation 17) decrease with radius, the ratio of the Alfvén to sound speed associated with a particular magnetic field strength increases with R and, as a result, the perturbations are damped at a weaker field for larger radii.

The maximum magnetic field strengths for which MRI unstable modes grow, as well as the range for which ν_{\max} is approximately the ideal-MHD rate, are summarized in Table 1 for the radii and disc structures of interest here. Note that, for the fiducial model, we obtained unstable modes at 1 au for $B \lesssim 8$ G. The growth rate is of the order of the ideal-MHD rate ($\nu = 0.75$) for $200 \text{ mG} \lesssim B \lesssim 5 \text{ G}$.

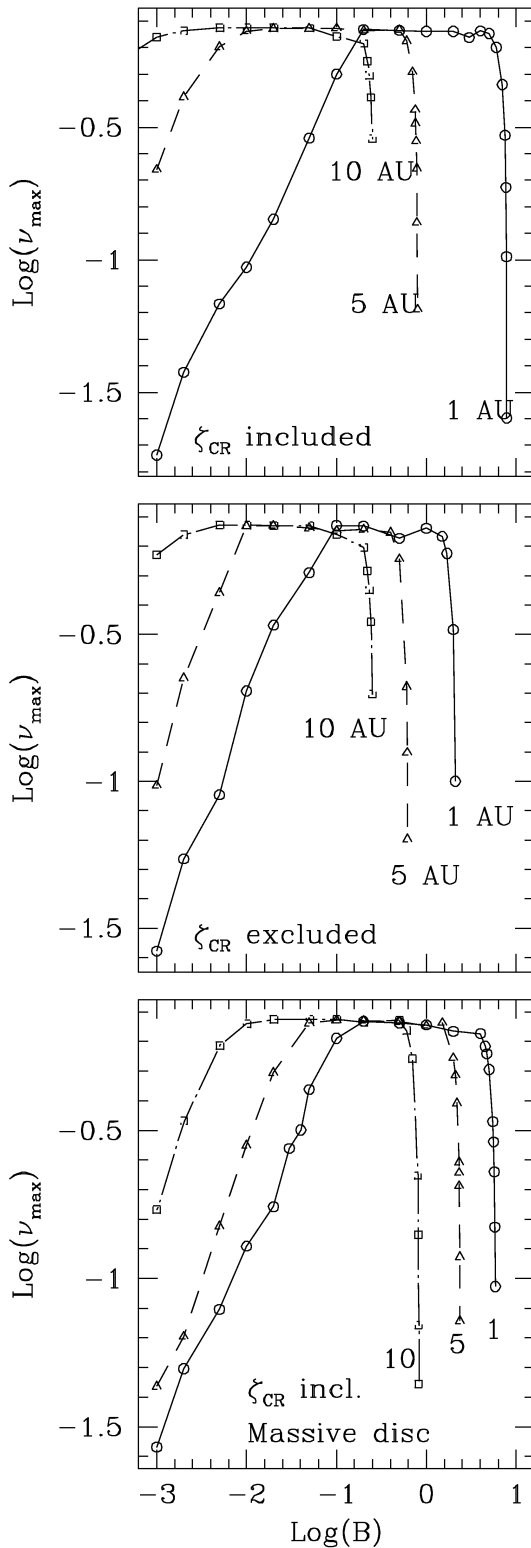


Figure 15. Growth rate of the most unstable modes of the MRI for $R = 1, 5$ and 10 au as a function of the strength of the magnetic field. Top and middle panels show results obtained with the fiducial model, assuming cosmic rays are either included, or excluded, from the disc. Bottom panel displays solutions obtained with the more massive disc, including cosmic ray ionization.

Table 1. Magnetic field strengths for which MRI perturbations grow at 1, 5 and 10 au for different disc models and sources of ionization. For the minimum-mass solar nebula disc, two sets of results are shown, where cosmic rays are either present or excluded from the disc. For the massive disc model, only the former case is presented. Columns labelled ‘ B_{\max} ’ list the maximum value of B for which each disc supports unstable MRI modes. Similarly, the ‘ $B(\nu \sim 0.75)$ ’ columns specify the subset of these for which perturbations grow at nearly the ideal-MHD rate ($\nu \sim 0.75$).

Radius (au)	Minimum-mass solar nebula				Massive disc	
	ζ_{CR} included	ζ_{CR} excluded	ζ_{CR} included	ζ_{CR} excluded	ζ_{CR} included	ζ_{CR} excluded
1	B_{\max}	$B(\nu \sim 0.75)$	B_{\max}	$B(\nu \sim 0.75)$	B_{\max}	$B(\nu \sim 0.75)$
5	7.85	0.2–5	2.10	0.1–1	5.85	0.2–0.5
10	0.80	0.02–0.5	0.62	0.01–0.05	2.36	0.05–0.5
	0.25	0.002–0.05	0.25	0.005–0.05	0.82	0.01–0.5

When cosmic rays are assumed to be excluded from the disc (see middle panel of Fig. 15 and central two columns of Table 1), unstable modes are obtained at 1 au only for $B \lesssim 2$ G. The corresponding range at 5 au is only slightly reduced and it is essentially the same as before at 10 au. This is consistent with our expectation that cosmic rays are a particularly important source of ionization at 1 au, where X-rays are excluded from the mid-plane. In this case, $\nu_{\max} \sim 0.75$ at 1 au for $100 \text{ mG} \lesssim B \lesssim 1$ G.

In the massive disc model (bottom panel of Fig. 15 and two right-most columns of Table 1), the MRI is active at 1 au for $B \lesssim 6$ G and $\nu_{\max} \sim 0.75$ for $200 \text{ mG} < B < 500 \text{ mG}$. For $R = 5$ and 10 au, MRI unstable modes exist in this disc for stronger fields than in the minimum-mass solar nebula model. This can be explained by recalling that the larger mass and column density translates, at these radii, into a larger gas pressure and a stronger equipartition magnetic field strength at the mid-plane. MRI modes are, as a result, damped for a stronger field than they are in the minimum-mass solar nebula model. On the contrary, for $R = 1$ au, the range of magnetic field strengths over which perturbations grow does not change appreciably, given the shielding of the inner sections at this radius.

6 DISCUSSION

In this paper, we have explored the vertical structure and linear growth of MRI perturbations of an initially vertical magnetic field, using a realistic ionization profile and assuming that ions and electrons are the sole charge carriers. This formulation is appropriate to model low-conductivity discs (Gammie & Menou 1998; Menou 2000; Stone et al. 2000) at late stages of accretion, after dust grains have settled into a thin layer around the mid-plane ($\sim 10^5$ yr, Nakagawa et al. 1981; Dullemond & Dominik 2004) and become dynamically uncoupled from the gas at higher z . Solutions were obtained at 1, 5 and 10 au from the central object as a function of the strength of the magnetic field for different configurations of the conductivity tensor, disc model and sources of ionization.

We have shown that the magnetic field is dynamically important in low-conductivity accretion discs over a wide range of field strengths. An example of this activity is the generation and sustaining of MRI-unstable modes, which are thought to be required to provide the angular momentum transport for accretion to proceed. The structure and growth rate of MRI perturbations are a function of the disc properties and the strength of the field. For a particular radius and disc model, they are a result of the competing action of different dominant conductivity components at different heights.

For R of the order of approximately a few au and relatively weak fields ($B \lesssim 100 \text{ mG}$ at 1 au or $B \lesssim 1 \text{ mG}$ at 5 au), the fluid close to

the mid-plane is in the Ohmic conductivity regime ($\sigma_{\parallel} \sim \sigma_2 \gg |\sigma_1|$, e.g. see Fig. 3). Conversely, for larger radii (or stronger fields) Hall conductivity dominates even at $z = 0$ (Wardle, in preparation; see also Section 4.3). Ambipolar diffusion dominates above this region until $\chi \sim 10$ (W99). For still higher z , the magnetic coupling is so strong that ideal MHD holds. The heights at which these transitions take place, for a particular disc model and radial position, are a function of the strength of the magnetic field. Note that, even when $|\sigma_1| \ll \sigma_2$, Hall diffusion still dominates the structure and growth of MRI modes when $\chi \lesssim \chi_{\text{crit}} \equiv |\sigma_1|/\sigma_{\perp}$ (SW03).

At 1 au, for the fiducial model, unstable modes exist for $B \lesssim 8$ G. For a significant subset of these strengths ($200 \text{ mG} \lesssim B \lesssim 5$ G), perturbations grow at about the ideal-MHD rate ($= 0.75\Omega$ in Keplerian discs). At this radius, Hall diffusion is locally dominant near the mid-plane for all magnetic field strengths for which MRI unstable modes exist. As a result, modes computed with a full conductivity tensor have a higher wavenumber and grow faster than perturbations obtained using the ambipolar diffusion approximation. On the other hand, ambipolar diffusion shapes the envelopes of these modes (especially for strong fields), causing them to peak at an intermediate height, instead of having the characteristic flat envelope that modes in the Hall limit have for these field strengths.

Cosmic rays are an important source of ionization at 1 au, given that X-rays do not reach the mid-plane at this radius (see Fig. 1). Consequently, if they are assumed to be excluded from the disc, the extent of the magnetically inactive dead zone about the mid-plane increases and unstable modes grow only for $B \lesssim 2$ G. Furthermore, under this assumption, perturbations obtained with a relatively strong initial magnetic field (e.g. $B \gtrsim 500$ mG), exhibit a kink in their amplitude. This feature is attributed to the sharp increase in the ionization fraction at the height where X-ray ionization becomes active. Finally, for the massive disc model ($\Sigma'_0 = 10\Sigma_0$ and $\rho'_0 = 10\rho_0$, incorporating cosmic ray ionization), the central dead zone extends to a higher z at 1 au, as the larger column density associated with this model causes the ionization fraction at low z to drop sharply (the disc is shielded from X-rays below $z/H \approx 2.6$ and even the cosmic ray ionization rate at the mid-plane is negligible). MRI perturbations grow in this case for $B \lesssim 6$ G, a range not significantly different from that of results in the fiducial model. This is the case because the effective surface density is largely unchanged, given the shielding of the inner sections.

At 5 au, for the fiducial model, MRI-unstable modes grow for $B \lesssim 800$ mG. When $20 \text{ mG} \lesssim B \lesssim 500$ mG, the growth rate is $\sim 0.75\Omega$. At this radius, Hall diffusion increases the growth rate and wavenumber of unstable modes for $B \lesssim 100$ mG, but for stronger fields, perturbations obtained with different configurations of the conductivity tensor have similar structures and growth rates, a signal that ideal-MHD conditions hold (Fig. 12). We also conducted an analysis of the effect of the alignment of the magnetic field and the angular velocity vector of the disc. Results indicate that, at this radius, the sign of $\sigma_1 B_z$ is important for $B \lesssim 10$ mG, the range of magnetic field strengths for which Hall diffusion is locally dominant at low z . As in the 1 au case, excluding cosmic rays reduces the range of magnetic field strengths for which MRI modes grow (unstable modes are found for $B \lesssim 600$ mG in this case) and there is a kink in the amplitude of the perturbations for $B \gtrsim 100$ mG. Finally, when the surface density of the disc is increased, the central dead zone occupies a larger cross-section, as expected and unstable modes are found for stronger fields than in the fiducial model. This is a result of the stronger equipartition magnetic field strength for this disc model at this radial position.

At 10 au, the MRI is active for $B \lesssim 250$ mG and the growth rate is close to the ideal-MHD rate for $2 \text{ mG} \lesssim B \lesssim 50$ mG. Furthermore, for $B \lesssim 10$ mG, perturbations obtained with a full conductivity tensor grow significantly faster than modes in the ambipolar diffusion limit, which reflects the contribution of the Hall effect (Fig. 14, bottom panel). At this radius, when cosmic rays are excluded, the range of magnetic field strengths for which unstable modes exist is not affected, given that X-rays are able to penetrate to the mid-plane. In the more massive disc, the extent of the dead zone increases, especially for weak fields ($B \lesssim 10$ mG) and perturbations grow for stronger fields than in the minimum-mass solar nebula disc.

The results just presented demonstrate how the properties of global (in the z direction) MRI unstable modes are dependent on the competing action of different conductivity regimes dominating at different heights. When the wavenumber is high, global effects (driven by the stratification of the disc) are less important and the structure of the modes is largely determined by local fluid conditions. In agreement with our previous paper (SW03), we find that, in this case, perturbations driven by Hall diffusion peak closer to the mid-plane than those where ambipolar diffusion is the dominant diffusion mechanism. Conversely, when global effects are important, the envelope of the perturbations is shaped by ambipolar diffusion while the Hall effect, which is typically important close to the mid-plane, increases the wavenumber and growth rate of the perturbations.

In the present formulation, it was assumed that ions and electrons are the only charge carriers. As discussed earlier, this is valid in late evolutionary stages of accretion, when dust grains have sedimented enough towards the mid-plane that they can be neglected when studying the dynamics of the gas at higher z . If grains are well mixed with the gas, however, recombinations on dust surfaces are expected to be dominant and $n_e \ll n_i$ (e.g. Wardle 2004; Desch 2004). The settling of dust grains is, consequently, a crucial factor in the overall equilibrium structure of discs. The time-scale for this settling to occur is expected to be affected by MHD turbulence. Although in quiescent discs dust grains may quickly settle into a thin sublayer about the mid-plane, the vertical stirring caused by MHD turbulence could potentially transport them back to higher vertical locations, preventing them from settling below a certain height (Dullemond & Dominik 2004 and references therein). It is also likely that the transition between vertical sections where dust grains are well mixed with the gas phase and those completely depleted of grains by settling is not ‘extremely sharp’ (Dullemond & Dominik 2004). The efficiency of this stirring is dependent on the disc being able to support MHD turbulence in the vertical locations where dust grains are present. On the other hand, dust grains can reduce the abundance of free electrons and the efficiency of MHD turbulence itself, by providing additional recombination pathways on their surfaces. Ultimately, the equilibrium structure of accretion discs will reflect the complex interplay between all these processes.

It is expected that the structure and growth of MRI unstable modes in such environments will be affected by the dependence of the ionization balance with height in the presence of chemistry taking place on grain surfaces. The study of the properties of the MRI in a disc where dust dynamics and evolution are determined consistently, and where Hall conductivity is taken into account, is essential to understand more fully the presence and efficiency of MRI-driven angular momentum transport in accretion discs. Non-ideal MHD simulations that explore the MRI non-linear stages as outlined above are of particular interest. Nevertheless, from the results presented in this paper, it is clear that Hall diffusion is crucial for the realistic modelling of the MRI in protostellar discs, particularly at a distance

of the order of a few au from the central object. More generally, Hall conductivity is an important factor when studying the magnetic activity of low-conductivity discs at these radii.

7 SUMMARY

We have presented in this paper the vertical structure and linear growth of the MRI in weakly ionized, stratified accretion discs, assuming an initially vertical magnetic field. Both the density and the conductivity are a function of height. Moreover, the conductivity is treated as a tensor and obtained with a realistic ionization profile. Two disc models were explored: the minimum-mass solar nebula disc (Hayashi 1981; Hayashi, Nakagawa & Nakazawa 1985) and a more massive disc, with the mass and surface density increased by a factor of 10.

This formulation is appropriate for the study of weakly ionized astrophysical discs, where the ideal-MHD approximation breaks down (Gammie & Menou 1998; Menou 2000; Stone et al. 2000). The ionization sources relevant here, outside the inner 0.1 au from the central object, are non-thermal: cosmic rays, X-rays and radioactive decay. For the minimum-mass solar nebula model, we compare solutions obtained including all three sources of ionization with those arrived at assuming that cosmic rays are excluded from the disc by the winds of the protostar. Recombination processes are taken to occur in the gas phase only, which is consistent with the assumption that dust grains have settled into a thin layer about the mid-plane, and ions and electrons are the only charge carriers. Perturbations of interest have vertical wavevectors ($k = k_z$) only, which are the most unstable modes (when initiated from a vertically aligned magnetic field) in both the Hall and Ohmic regimes (Balbus & Hawley 1991; Sano & Miyama 1999). This is not necessarily the case in the ambipolar diffusion limit (Desch 2004; Kunz & Balbus 2004), where the fastest growing modes can have radial as well as vertical wavenumbers. Under the adopted approximations, the properties of the MRI in the ambipolar diffusion and Ohmic conductivity limits are identical.

Three parameters were found to control the dynamics and evolution of the fluid:

- (i) the local ratio of the Alfvén to sound speed (v_A/c_s);
- (ii) the local coupling between ionized and neutral components of the fluid (χ), which relates the frequency at which non-ideal effects are important with the dynamical (Keplerian) frequency of the disc; and
- (iii) the ratio of the components of the conductivity tensor perpendicular to the magnetic field (σ_1/σ_2), which characterizes the conductivity regime of the fluid.

These parameters were evaluated at $R = 1, 5$ and 10 au for a range of magnetic field strengths. The linearized system of ODE was integrated from the mid-plane to the surface of the disc under appropriate boundary conditions, and solutions were obtained for representative radial locations of the disc as a function of the magnetic field strength and for different configurations of the conductivity tensor.

The main results of this study are summarized below.

- (i) Results for the minimum-mass solar nebula model, incorporating cosmic ray ionization (the fiducial model) are as follows. At 1 au, unstable MRI modes exist for $B \lesssim 8$ G. When $200 \text{ mG} \lesssim B \lesssim 5$ G, the most unstable modes grow at approximately the ideal-MHD rate ($= 0.75\Omega$). Hall diffusion dominates the structure and growth rate of unstable modes for all magnetic field strengths for which they grow. For strong fields, ambipolar diffusion shapes the envelope of the perturbations, which peak at an intermediate

height. Finally, at this radius, a magnetically dead zone (Gammie 1996; Wardle 1997) exists when $B < 1$ G. As expected, the vertical extent of this zone decreases when the magnetic field gets stronger. It increases when a more massive disc model is used.

At 5 au, MRI-unstable modes grow for $B \lesssim 800$ mG and the growth rate is close to the ideal-MHD rate for $20 \text{ mG} \lesssim B \lesssim 500$ mG. Perturbations incorporating Hall conductivity have a higher wavenumber and grow faster than solutions in the ambipolar diffusion limit for $B \lesssim 100$ mG. When $B \lesssim 10$ mG, the structure and growth of full σ perturbations are dependent on the alignment of the magnetic field and angular velocity vectors of the disc. Unstable modes grow even at the mid-plane for $B \geq 100$ mG, but for weaker fields, a small dead region exists.

At 10 au, the MRI is active for $B \lesssim 250$ mG. The growth rate is close to the ideal-MHD rate for $2 \text{ mG} \lesssim B \lesssim 50$ mG and when $B \lesssim 10$ mG, perturbations obtained with a full conductivity tensor grow significantly faster than modes in the ambipolar diffusion limit. Modes show only a very small dead region when $B \sim 1$ mG.

(ii) When the magnetic field is weak (e.g. $B \lesssim 200$ mG at 1 au), the maximum growth rate of unstable MRI modes (ν_{\max}) increases with the strength of the magnetic field, a feature driven by ambipolar diffusion.

(iii) When cosmic rays are assumed to be excluded from the disc, unstable modes at 1 au grow only for $B \lesssim 2.1$ G. Results at 5 au only change slightly, while solutions at 10 au are not affected at all, as expected.

(iv) For the massive disc model ($\Sigma'_0 = 10\Sigma_0$ and $\rho'_0 = 10\rho_0$, incorporating cosmic ray ionization), MRI perturbations grow for stronger fields at 5 and 10 au, in relation to the minimum-mass solar nebula model. Results at 1 au are unchanged, given that in this case the effective surface density is not significantly different.

MRI perturbations grow in protostellar discs for a wide range of fluid conditions and magnetic field strengths. Hall diffusion largely determines the structure and growth rate of perturbations at radii of the order of a few au from the central protostar. This indicates that, despite the low magnetic coupling, the magnetic field is dynamically important in low-conductivity astrophysical discs and will impact the dynamics and evolution of these discs.

ACKNOWLEDGMENTS

We are thankful to the referee for useful feedback. We also thank Arie König for pointing out the correct criterion for radiative recombination to dominate the ionization balance. This research has been supported by the Australian Research Council. RS acknowledges support by an Australian Postgraduate Award and partial support from NASA Theoretical Astrophysics Program Grant NNG04G178G.

REFERENCES

- Balbus S. A., 2003, *ARA&A*, 41, 555
- Balbus S. A., Hawley J. F., 1991, *ApJ*, 376, 214
- Balbus S. A., Hawley J. F., 1998, *Rev. Mod. Phys.*, 70, 1
- Balbus S. A., Papaloizou J. C. B., 1999, *ApJ*, 521, 650
- Balbus S. A., Terquem C., 2001, *ApJ*, 552, 235
- Blaes O. M., Balbus S. A., 1994, *ApJ*, 421, 163
- Consolmagno G. J., Jokiipii J. R., 1978, *Moon Planets*, 19, 253
- Desch S. J., 2004, *ApJ*, 608, 509
- Draine B. T., Roberge W. G., Dalgarno A., 1983, *ApJ*, 264, 485
- Dullemond C. P., Dominik C., 2004, *A&A*, 421, 1075
- Fleming T. P., Stone J. M., Hawley J. F., 2000, *ApJ*, 530, 464

- Fromang S., Terquem C., Balbus S. A., 2002, *MNRAS*, 329, 18
- Gammie C. F., 1996, *ApJ*, 457, 355
- Gammie C. F., Balbus S. A., 1994, *MNRAS*, 270, 138
- Gammie C. F., Menou K., 1998, *ApJ*, 492, L75
- Glassgold A. E., Feigelson E. D., Montmerle T., 2000, in Mannings V. G., Boss A. P., Russell S., eds, *Protostars & Planets IV*. Univ. Arizona Press, Tucson, p. 429
- Hawley J. F., Balbus S. A., 1991, *ApJ*, 376, 223
- Hawley J. F., Balbus S. A., 1995, *Publ. Astron. Soc. Aust.*, 12, 159
- Hawley J. F., Stone J. M., 1998, *ApJ*, 501, 758
- Hayashi C., 1981, *Prog. Theor. Phys. Supp.*, 70, 35
- Hayashi C., Nakasawa K., Nakagawa Y., 1985, in Black D. C., Mathews M. S., eds, *Protostars & Planets II*. Univ. Arizona Press, Tucson, p. 1100
- Igea J., Glassgold A. E., 1999, *ApJ*, 518, 848
- Jin L., 1996, *ApJ*, 457, 798
- Kitamura Y., Momose M., Yokogawa S., Kawabe R., Tamura M., 2002, *ApJ*, 581, 357
- Kunz M., Balbus S. A., 2004, *MNRAS*, 348, 355
- Lin D. N., Papaloizou J. C., 1980, *MNRAS*, 191, 37
- MacLow M. M., Norman M. L., Königl A., Wardle M., 1995, *ApJ*, 442, 726
- Mathis J. S., Rumpl W., Nordsieck K. H., 1977, *ApJ*, 217, 425
- Menou K., 2000, *Sci*, 288, 2022
- Morton D. C., 1974, *ApJ*, 193, L35
- Nakagawa Y., Nakazawa K., Hayashi C., 1981, *Icarus*, 45, 517
- Nakano T., Umebayashi T., 1986, *MNRAS*, 218, 663
- Nishi R., Nakano T., Umebayashi T., 1991, *ApJ*, 368, 181
- Oppenheimer M., Dalgarno A., 1974, *ApJ*, 192, 29
- Papaloizou J. C. B., Terquem C., 1997, *MNRAS*, 287, 771
- Pilipp W., Hartquist T. W., Havnes O., Morfill G. E., 1987, *ApJ*, 314, 341
- Salmeron R., Wardle M., 2003, *ApJ*, 345, 992 (SW03)
- Sano T., Miyama S., 1999, *ApJ*, 515, 776
- Sano T., Stone J. M., 2002a, *ApJ*, 570, 314
- Sano T., Stone J. M., 2002b, *ApJ*, 577, 534
- Sano T., Stone J. M., 2003, *ApJ*, 586, 1297
- Sano T., Inutsuka S. I., Miyama S. M., 1998, *ApJ*, 506, L57
- Sano T., Miyama S., Umebayashi J., Nakano T., 2000, *ApJ*, 543, 486
- Sano T., Inutsuka S. I., Turner N. J., Stone J. M., 2004, *ApJ*, 605, 321
- Shull J. M., Van Steenberg M. E., 1985, *ApJ*, 298, 268
- Spitzer L., 1978, *Physical Processes in the Interstellar Medium*. Wiley, New York
- Stone J. M., Fleming T., 2003, *ApJ*, 585, 908
- Stone J. M., Gammie C. F., Balbus S. A., Hawley J. F., 2000, in Mannings V. G., Boss A. P., Russell S., eds, *Protostars & Planets IV*. Univ. Arizona Press, Tucson, p. 589
- Toomre A., 1964, *ApJ*, 139, 1217
- Umebayashi T., Nakano T., 1980, *PASJ*, 32, 405
- Umebayashi T., Nakano T., 1981, *PASJ*, 33, 617
- Umebayashi T., Nakano T., 1990, *MNRAS*, 243, 103
- Voit M., 1991, *ApJ*, 377, 158
- Wardle M., 1997, in Wickramasinghe D., Ferrario L., Bicknell G., eds, *Proc. IAU Colloq. 163, Accretion Phenomena and Related Outflows*. Astron. Soc. Pac., San Francisco, p. 561
- Wardle M., 1998, *MNRAS*, 298, 507
- Wardle M., 1999, *MNRAS*, 307, 849 (W99)
- Wardle M., 2004, *Ap&SS*, 291, 317
- Wardle M., Ng C., 1999, *MNRAS*, 303, 239
- Weidenschilling S. J., Cuzzi J. N., 1993, in Levy E. H., Lunine J. I., eds, *Protostars & Planets III*. Univ. Arizona Press, Tucson, p. 1031

This paper has been typeset from a $\text{\TeX}/\text{\LaTeX}$ file prepared by the author.